LETTER

Self-reporting and self-regulating liquid crystals

Young-Ki Kim[1], Xiaoguang Wang[1,2], Pranati Mondkar[1], Emre Bukusoglu[1,3] & Nicholas L. Abbott[1]*

Liquid crystals (LCs) are anisotropic fluids that combine the long-range order of crystals with the mobility of liquids[1,2]. This combination of properties has been widely used to create reconfigurable materials that optically report information about their environment, such as changes in electric fields (smart-phone displays)[3], temperature (thermometers)[4] or mechanical shear[5], and the arrival of chemical and biological stimuli (sensors)[6,7]. An unmet need exists, however, for responsive materials that not only report their environment but also transform it through self-regulated chemical interactions. Here we show that a range of stimuli can trigger pulsatile (transient) or continuous release of microcargo (aqueous microdroplets or solid microparticles and their chemical contents) that is trapped initially within LCs. The resulting LC materials self-report and self-regulate their chemical response to targeted physical, chemical and biological events in ways that can be preprogrammed through an interplay of elastic, electrical double-layer, buoyant and shear forces in diverse geometries (such as wells, films and emulsion droplets). These LC materials can carry out complex functions that go beyond the capabilities of conventional materials used for controlled microcargo release, such as optically reporting a stimulus (for example, mechanical shear stresses generated by motile bacteria) and then responding in a self-regulated manner via a feedback loop (for example, to release the minimum amount of biocidal agent required to cause bacterial cell death).

We use nematic phases as representative LCs. Nematic LC phases comprise molecules that assume a preferred orientation, called the director $\boldsymbol{n}$[1]. This leads to anisotropic optical properties (birefringence) and elasticity, the latter allowing energy to be stored in strained states of LCs at rest (for example, via bending, splaying or twisting)[1,2]. When a dispersed microphase of an immiscible liquid, solid or gas (guest) is introduced into an LC host, the ordering of LCs around the guest microphase is determined by a competition between the elastic energy (KR) arising from the strain of the LC and an orientation-dependent interfacial energy at the LC–guest interface (WR^2), where K is the Frank elastic constant of the LC, W is the surface-anchoring energy density and R is the radius of the guest[2,8,9]. If $WR^2 > KR$ (that is, $R > K/W$), the guest will elastically strain the LC and thus can generate a strong repulsive force (elastic repulsion, F_e) between the guest and the boundaries of the nematic LC (Fig. 1a)[10–12]. The strain and associated topological defects will also mediate interactions between guest microphases, which can prevent contact or coalescence of liquid microphases[10–14]. For typical nematic LCs formed from small organic molecules (thermotropic LCs), $K \approx 10^{-12}$ N and $W \approx 10^{-6}$ J m^{-2} (ref. 8); thus, $K/W \approx 1\,\mu$m and the associated elastic energy is about 2,400$k_B T$ (Methods), where k_B is the Boltzmann constant and T is the temperature. In the absence of external forces, therefore, we predict that dispersed microphases with $R \geq K/W$ would be sequestered by elastic forces within a bulk nematic phase and prevented from escaping into the surrounding environment.

To demonstrate the elastic trapping of guest microphases in LCs, we dispersed aqueous microdroplets ($0.5\,\mu$m $\leq R \leq 3\,\mu$m) containing a model chemical solute (a red dye for visualization) and the surfactant sodium dodecyl sulphate (SDS) in nematic 4′-pentyl-4-biphenylcarbonitrile (5CB; Fig. 1a), and then filled a mini-well (3.5 mm in depth)

with the dispersion (Fig. 1b). The SDS adsorbed at the interface between the aqueous microdroplets and the LC and aligned $\boldsymbol{n}$ perpendicular to the local droplet interface; this is called homeotropic anchoring[7]. Accordingly, each aqueous microdroplet was surrounded by a region of strained LCs that included a point topological defect (called a hyperbolic hedgehog[10–14]; Fig. 1a). At the interface between the LC and the overlying bulk aqueous phase, the LC adopted a parallel orientation (planar anchoring), leading to a bright optical appearance of the system (left inset in Fig. 1e). As shown in Fig. 1c and Extended Data Fig. 1, the aqueous environment contacting the LC remained free of red tracer after four days at room temperature. This result is consistent with the effects of the elastic repulsion[10–12] of the guest microdroplets away from the interface between the LC and the overlying aqueous phase by a force $F_{e1} = -A^2 B\pi K[R/(h_1 + R)]^4$, where A is a numerical factor ($A = 0$ for $R < K/W$ or for an isotropic phase[10,11]), B is an anchoring-dependent constant ($B = 3/4$ and $B = 1/2$ for the parallel and perpendicular orientation, respectively, of $\boldsymbol{n}$ at the interface between the LCs and the bulk aqueous phase) and h_1 is the distance between the microdroplet surface and the LC interface to the bulk aqueous phase (Fig. 1a). The trapping of microdroplets within LCs was observed to occur regardless of the relative density of the microdroplets (ρ_{aq}) and the LCs (ρ_{LC}) because F_{e1} is much larger than buoyant forces (F_b) at room temperature; for $R = 3\,\mu$m and 5CB, $|F_{e1}/F_b| > 500$ at $h_1/R < 1$ (Methods).

Thermal and chemical stimuli can trigger optical responses in LCs via changes in LC ordering[2,4,6–8,15]. For example, 5CB undergoes a first-order transition from a nematic (N) to an isotropic (I) phase at temperature $T_{NI}^{5CB} = 35$ °C. Alternatively, isothermal phase transitions can be induced by absorption of solutes[16]. We found that heating of 5CB containing microdroplets to $T_h > 35$ °C from below (through contact with a warm body) led not only to an N-to-I phase transition accompanied by an optical response of the LCs (bright to dark; see insets and dashed line in Fig. 1e), but also to the ejection of microdroplets and red tracer into the overlying aqueous environment (Fig. 1d and solid line in Fig. 1e). The release occurred irrespective of the relative magnitudes of ρ_{aq} and ρ_{LC}, including in conditions under which the microdroplets sediment downwards and away from the interface to the overlying aqueous environment ($\rho_{aq} > \rho_{LC}$). Surprisingly, the release was transient, coinciding with the time period of the phase transition (Fig. 1e). After the phase transition, we did not measure any additional release for a period of 24h (Extended Data Fig. 1). A second pulse of solute was released when the system was cooled back to $T_c = 25$ °C to reform the birefringent N phase (Fig. 1f). We subsequently repeated the heating and cooling cycles and observed that, with each optical response, a well defined pulse of microdroplets was ejected into the overlying aqueous phase (Fig. 1g). After 20 cycles, the mass of solute dispensed into the aqueous environment was linearly proportional to the initial concentration of aqueous microdroplets, C_{aq}, in the LCs (Fig. 1h, i), revealing a high level of control. Thermal release was also conveniently initiated by ohmic heating of a thin, electrically resistive film supporting the LCs (Extended Data Fig. 1).

We determined that the pulsatile ejection of microdroplets accompanied the upward motion of the N–I interface towards the overlying aqueous environment (Extended Data Fig. 1). Microscopic observations revealed that repulsive elastic interactions between the aqueous

[1]Department of Chemical and Biological Engineering, University of Wisconsin-Madison, Madison, WI, USA. [2]Present address: John A. Paulson School of Engineering and Applied Sciences, Harvard University, Cambridge, MA, USA. [3]Present address: Chemical Engineering Department, Middle East Technical University, Ankara, Turkey. *e-mail: nlabbott@wisc.edu
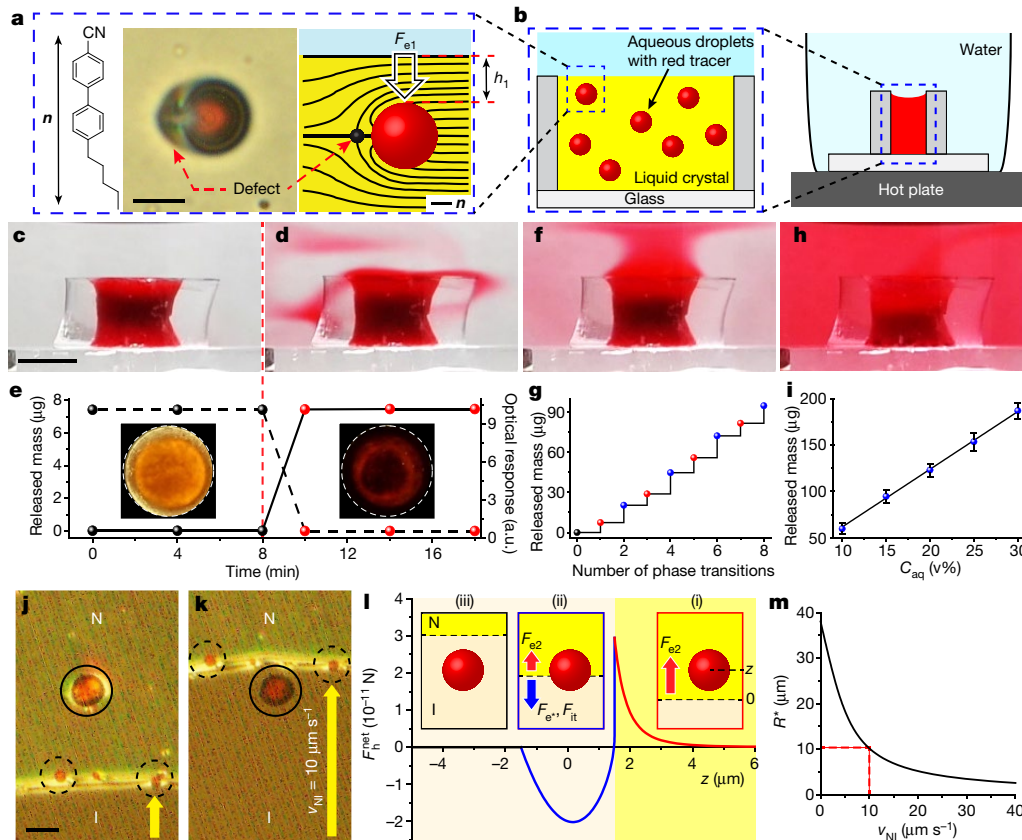
Fig. 1 | Pulsatile ejection of microdroplets from LCs and accompanying LC optical responses, as triggered by N–I phase transitions. a, Molecular structure of 5CB and optical micrograph (bright field) of an aqueous microdroplet (containing 9 mM of SDS and red tracer) in nematic 5CB with a reconstructed LC director profile. F_{e1} is the repulsive elastic force acting between the aqueous microdroplet and the interface between the LC and the overlying aqueous phase. Scale bar, 10 μm. **b**, Illustration of a dispersion of aqueous microdroplets in an LC that is hosted in a mini-well and submerged under a bulk aqueous phase that is initially free of tracer. **c, d, f, h**, Sequential photographs of the LC-filled mini-well containing the initial N phase (**c**) and after N-to-I (**d**), N-to-I-to-N (**f**) and 10 phase transitions (**h**); see Supplementary Video 1. The phase transitions were triggered by heating and cooling between 25 °C and 50 °C. Scale bar, 3 mm. **e**, Mass of tracer released (solid line) from LC as a function of time before (black circles) and after N-to-I phase transition (red circles); the accompanying optical response of the LC is shown by the dashed line. The insets show micrographs of mini-wells (of diameter 3 mm) between crossed polars (top view). **g**, Mass of tracer released as a function of the

number of phase transitions. Red and blue circles indicate mass released after N-to-I and I-to-N phase transitions, respectively. a.u., arbitrary units. **i**, Mass of tracer released after 20 phase transitions as a function of the microdroplet concentration (C_{aq}) initially in the LC. The data points show mean values and the error bars represent 1 s.d. ($n > 3$). **j, k**, Sequential micrographs showing the transport of small (dashed circles; $R < R^*$), but not of large (solid circles; $R > R^*$), microdroplets by a moving N–I interface (yellow arrows; $v_{NI} = 10\,\mu m\,s^{-1}$) upon heating. Scale bar, 20 μm. **l**, Calculated net force F_h^{net} acting on a microdroplet ($R = 1.5\,\mu m$) near an N–I interface. The insets show microdroplets for $z \geq R$ (red line), $-R < z < R$ (blue line), and $z \leq -R$ (black line). Red and blue arrows indicate the forces that favour and oppose the ejection of microdroplets, respectively. F_{e2} is the repulsive elastic force acting between the aqueous microdroplet dispersed in the N phase and the N–I interface, which is modified by the elastic force F_{e^*} and interfacial tension force F_{it} when the aqueous microdroplet penetrates that N–I interface (Methods). **m**, Calculated dependence of R^* on v_{NI}. The red dashed line indicates R^* at $v_{NI} = 10\,\mu m\,s^{-1}$, which coincides with the experimental conditions.

microdroplets and the moving N–I interface pushed the microdroplets ahead of the interface in a manner that depended on the size of the microdroplets (Fig. 1j, k). Past studies[17] have observed N–I interfaces to transport adsorbed colloids, but they have not reported the elastic levitation of colloids ahead of an N–I interface, as is required for triggering the release of the microdroplet shown in Fig. 1. The elastic force—evaluated as $F_{e2} = +A^2 B\pi K(R/z)^4$, where $B = 3/4$ and z is the vertical position of the centre of the microdroplet relative to an N–I interface ($z = 0$)—elastically levitates the microdroplets to a height defined by the net force $F_h^{net}(z) = 0$ above the N–I interface (see Fig. 1l and Methods)[11]. In the absence of F_{e2}, the microdroplets will not be transported by the rising N–I interface. Microdroplets pushed by F_{e2} ahead of the moving N–I interface also experience a downward Stokes drag force $F_S = -6\pi\eta_{LC}v_{aq}R$, where η_{LC} is the dynamic viscosity of the LC and v_{aq} is the velocity of the microdroplet[18] (which is equal to the velocity v_{NI} of the moving N–I interface for microdroplets transported by the N–I interface). If F_S exceeds the maximum value of $F_h^{net}(z)$ (Fig. 1l), microdroplets break through the moving N–I interface. For $(z-R)/R \ll 1$, F_{e2} is independent of R, whereas F_S scales linearly with R;

thus, for each value of v_{NI}, our model defines a critical microdroplet radius R^* above which microdroplets are not transported by the moving N–I interface (Fig. 1m and Extended Data Fig. 2). Our model predicts $R^* = 10.2\,\mu m$ for $v_{NI} = 10\,\mu m\,s^{-1}$ (Fig. 1m), in good agreement with our experiments (Fig. 1j, k; $R^* = 10 \pm 1\,\mu m$). Our model also predicts that microdroplets with $R = 1.5\,\mu m$ pushed by an N–I interface with $v_{NI} = 10\,\mu m\,s^{-1}$ will be able to reach within 60 nm of the interface of an overlying aqueous phase. At this separation, attractive interfacial forces, such as van der Waals and electrical double-layer forces (see below), mediate the fusion of the microdroplets with the overlying aqueous phase (Extended Data Fig. 3).

Modified versions of the above-described elastostatic model can account for the ejection of microdroplets by the upward motion of the N–I interface during cooling (Methods and Extended Data Fig. 4). In addition, the model predicts that tuning of the elastic properties of the LC, which can be achieved using light[19], temperature[19,20] and chemical additives[6,7,16], can trigger optical responses in LCs along with a continuous release of microdroplets; these predictions were verified by experiments (see Extended Data Figs. 5–7 and Methods).
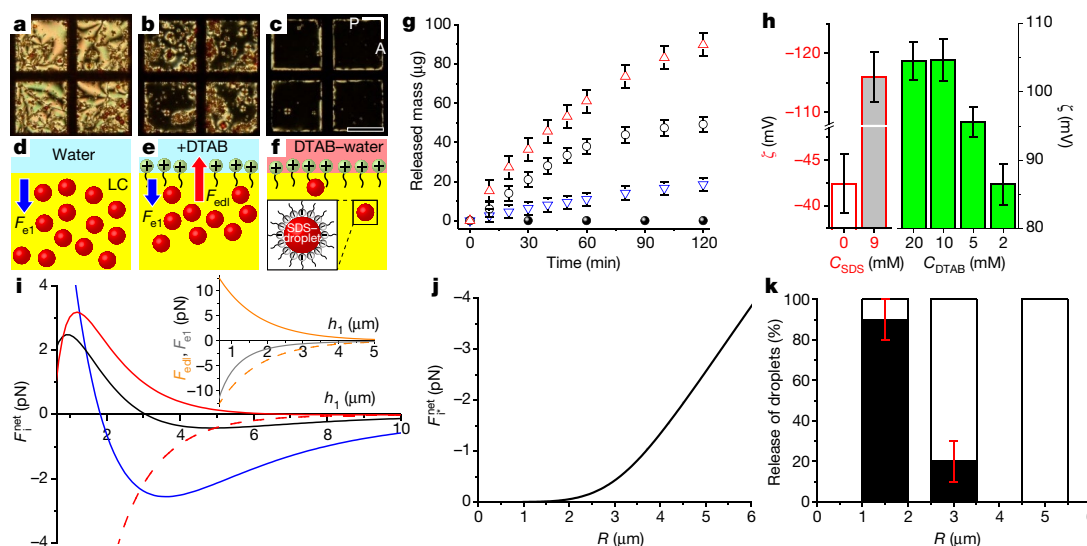
Fig. 2 | Isothermal triggering of release of microdroplets dispersed in LCs by interfacial charge interactions. a–f, Sequential micrographs (crossed polars, top view, **a–c**) and corresponding illustrations (side view, **d–f**) of an LC film (thickness 40 μm, hosted in a square grid) containing microdroplets (concentration $C_{SDS} = 9$ mM and red tracer) before (**a, d**) and after addition of the cationic amphiphile DTAB (10 mM) to the overlying aqueous phase, at 0 (**b, e**) and 60 min (**c, f**). P and A indicate the orientations of the polarizer and analyser, respectively. Red and blue arrows indicate the forces that favour (electrical double-layer force, F_{edl}) and oppose (elastic repulsion, F_{el}) the ejection of microdroplets, respectively. Green (in **e, f**) and white (inset in **f**) circles with tails represent cationic (DTAB) and anionic (SDS) surfactants, respectively. Scale bar, 200 μm. **g**, Mass of tracer released from the LC following the addition of DTAB at concentrations $C_{DTAB} = 2$ mM (upside-down triangles), 5 mM (empty circles), 10 mM (triangles) or SDS at $C_{SDS} = 5$ mM (full circles) to

the overlying aqueous phase. The symbols show mean values and the error bars are 1 s.d. ($n > 5$). **h**, Zeta potentials (ζ) of LC–aqueous interfaces without amphiphiles (white bar) and with SDS (grey bar) or DTAB (green bars). Data show mean values and the error bars are 1 s.d. ($n > 3$). **i**, Calculated net force ($F_i^{net} = F_{edl} + F_{el}$) acting on a microdroplet ($C_{SDS} = 9$ mM) with $R = 1.5$ μm (red), 3 μm (black) and 5 μm (blue) after the addition of DTAB (10 mM; solid lines) or SDS (5 mM, $R = 1.5$ μm; red dashed line) to the overlying aqueous phase, plotted as a function of h_1. The inset shows the corresponding elastic (F_{el}; grey) and electrical double-layer (F_{edl}; orange dashed and solid lines are for $C_{SDS} = 5$ mM and $C_{DTAB} = 10$ mM in the overlying aqueous phase, respectively) forces for $R = 1.5$ μm. **j**, Magnitude (F_{i*}^{net}) of the kinetic barrier in **i** as a function of R. **k**, Measured fraction of microdroplets released with $R = 1–2$ μm, 2.5–3.5 μm and 4.5–5.5 μm. Data are mean values and error bars are 1 s.d. ($n > 10$).

The orientations of LCs respond to interfacial interactions, which can be modulated by the adsorption of specific synthetic and biological molecules, as well as chemical transformations (for example, enzymatic or photochemical) of adsorbed species[6,7]. We found that specific interfacial events can introduce interactions (for example, interfacial charge interactions) that override the elastic trapping of microdroplets. For example, at room temperature, microdroplets containing anionic amphiphile (SDS) and solutes were elastically trapped within supported films of 5CB (thickness, 40 μm) immersed under an aqueous phase (Fig. 2a, d). The LC films have bright optical appearances due to the planar anchoring of the LCs at the interface to the bulk aqueous phase. However, addition of a cationic amphiphile (dodecyltrimethylammonium bromide; DTAB) to the bulk aqueous environment triggered an LC anchoring transition to a homeotropic orientation. The anchoring transition caused an optical response from the LC (bright to dark; see Fig. 2a, b) and the release of microdroplets into the overlying aqueous phase (Fig. 2a–g). By contrast, addition of anionic amphiphiles to the overlying aqueous phase did not trigger release of microdroplets (Fig. 2g). The rate of microdroplet release was correlated closely with the zeta potential, ζ, of the interface between the LC and aqueous phase, which is controlled by addition of charged amphiphiles (Fig. 2g, h). These observations indicate that release of microdroplets is triggered by electrical double-layer forces[21] (F_{edl}) acting between the microdroplets and the interface between the LC and the bulk aqueous phase. These forces can overcome the elastic forces (F_{el}) that trap the microdroplet initially. We evaluated the double-layer forces as $F_{edl} = -4\pi\varepsilon_0\varepsilon(R/\lambda)(k_BT/e_c)^2 Y_pY_i \, e^{-h_1/\lambda}$, where λ is the Debye screening length, ε is the relative dielectric constant measured along the interface normal, ε_0 is the vacuum permittivity, e_c is the elementary charge, and Y_p and Y_i are the effective surface potentials of the microdroplet and the LC interface, respectively (see Methods). The calculated net

force ($F_i^{net} = F_{edl} + F_{el}$) experienced by microdroplets near the LC interface confirmed that addition of DTAB generates an attractive F_{edl} that overcomes the repulsive F_{el} (Fig. 2i). We also found a strong correlation between ζ, F_{edl} and the microdroplet release rate (Extended Data Fig. 8). We examined the influence of microdroplet size (R) on F_i^{net} and the experimental release of microdroplets. In the limit of $h_1 \ll R$ (close approach), larger microdroplets experience a larger attractive F_i^{net} due to F_{edl} (in this limit, F_{el} is independent of R whereas F_{edl} scales linearly with R). Importantly, however, the distance dependence of F_{el} and F_{edl} leads to a repulsive kinetic barrier ($F_{i*}^{net} < 0$) that grows with R (Fig. 2i, j). Specifically, our model predicts that a kinetic barrier will prevent ejection of microdroplets with $R > 2.3$ μm. Our experimental observations confirmed the existence of the size-dependent kinetic barrier (Fig. 2k). The role of interfacial charge in triggering microdroplet release was also confirmed by experiments involving changes in pH and the adsorption of polyelectrolytes (Extended Data Fig. 8). In addition, we demonstrated that adsorption of anionic bacterial lipopolysaccharides (Extended Data Fig. 9) can introduce interfacial charge interactions that trigger changes in the optical appearance of LCs and the release of microdroplets containing anti-bacterial agents (for example, DTAB) from the LCs.

Past studies[1–5] have demonstrated that interfacial shear stresses can change the orientations of LCs; here we show that this leads to changes in both $F_{edl}(\varepsilon)$ and $F_{el}(B)$ due to the orientation dependence of ε and B, respectively. The orientation of the LC director changes when interfacial shear stresses exceed the elastic torque required to rotate the LC (which is approximately equal to $K(\partial^2\Psi/\partial d^2)$, where Ψ is the angle of the LC director from the surface normal and d is distance from the LC interface[15]). For a typical nematic LC ($K \approx 10^{-12}$ N), we calculate that an interfacial shear stress of 1 N m^{-2} is sufficient to reorient the LC director within an interfacial layer with thickness of about 10^{-6}
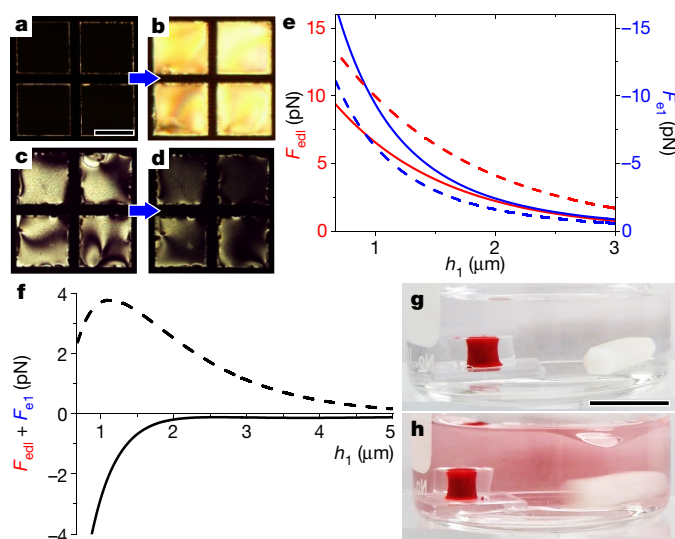
Fig. 3 | Optical response of LCs and release of microdroplets from LCs, as triggered by interfacial shear stresses. a–d, Optical response of LC films (of thickness 40 μm, hosted in a square grid supported on a treated-glass slide; crossed polars) with initially homeotropic (**a**, **b**; achieved using 2 mM SDS in the aqueous phase) or planar (**c**, **d**; surfactant-free aqueous phase) anchoring at the interface of the LCs with the overlying aqueous phase, before (**a**, **c**) and after (**b**, **d**) the introduction of interfacial shear stress via convection in the aqueous phase. Scale bar, 200 μm. **e**, **f**, Calculated F_{edl} (**e**; red lines), F_{e1} (**e**; blue lines) and net force (**f**; black lines) for an aqueous microdroplet ($R = 1.5$ μm) containing $C_{DTAB} = 2$ mM ($\zeta = 90$ mV; Fig. 2h), with planar (solid lines) or homeotropic (dashed lines) orientation of the LC at its interface (with $\zeta = -42.5$ mV) with the overlying aqueous phase. **g**, **h**, Sequential photographs showing the ejection of microdroplets ($C_{DTAB} = 2$ mM and red tracer) from the LCs, which is triggered by interfacial shear stresses, before (**g**) and after (**h**) stirring the overlying water with a magnetic bar for 30 min to generate an interfacial shear stress of about 10 N m⁻². Scale bar, 1 cm.

m (as seen in our experiments). In agreement with this calculation, we observed aqueous phases sheared at 10^4 s⁻¹ to generate interfacial shear stresses of about 10 N m⁻² (the viscosity of water is 10^{-3} kg m⁻¹ s⁻¹) that triggered changes in the orientations and optical responses of LC films with initially homeotropic (Fig. 3a, b) or planar (Fig. 3c, d) orientations. When the initial orientation of the LC at its interface with the overlying aqueous phase was planar, we observed microdroplets containing cationic surfactant (with concentration $C_{DTAB} = 2$ mM) to be elastically trapped within the LC, consistent with our calculation that the attractive F_{edl} cannot overcome the repulsive F_{e1} (solid lines in Fig. 3e, f); we evaluated F_{edl} and F_{e1} using $\varepsilon = 13.2$, $B = 3/4$ and $\zeta = -42.5$ mV at the interface between the LC and the overlying aqueous phase (Fig. 2h). The presence of mechanical shear at the interface, however, caused the orientation of the LC to deviate from the initial planar orientation (Fig. 3c, d; see also Fig. 4), which changed the balance of orientation-dependent elastic and electrical double-layer forces. For the limiting case of a fluctuation to a perpendicular orientation ($\varepsilon = 19.7$ and $B = 1/2$), we calculated the increase in F_{edl} and decrease in F_{e1} to be sufficient to trigger ejection of microdroplets (see dashed lines in Fig. 3e, f and Methods). This prediction was confirmed by experiments showing that microdroplet release was triggered by the interfacial shear stresses (> 10 N m⁻²) generated by shearing the overlying aqueous phase with a magnetic bar (Fig. 3g, h).

Conventional materials used for controlled release of small or large molecules do not self-report triggering events, have not been shown to respond to the same combinations of physical, chemical and biological stimuli that we describe here, and do not permit programming of the diversity of dynamic responses (for example, pulsatile or continuous release), including self-regulating responses. For example, guided by the results shown in Fig. 1, we designed a cholesteric (chiral nematic)[22]

LC system that was triggered by the touch of a human finger (Fig. 4a–d; Supplementary Video 2). An N-to-I phase transition, which was designed to occur upon exposure to physiological temperature, triggered a change in the Bragg diffraction of light (as used in electronic paper[3] and LC thermometers[4]), and elastic forces F_{e2} generated ahead of the N–I interface ejected a precise dose of chemical microcargo (a dye for visualization and a cleaning agent). We note that the twisted LC within the cholesteric phase modifies the magnitude of F_e relative to an achiral nematic phase, but does not eliminate the force required to eject microcargo[23]. The programmed release of precise doses of microcargo upon thermal activation differs from the behaviour of conventional materials that release chemical agents continuously upon thermal activation until the stimulus is removed or the agent reservoir is exhausted (for example, thermally responsive hydrogels[24] and lyotropic LC matrices[25]). Current methods that release precise and repeated doses of active agent require the use of devices incorporating micrometre-scale chips, pumps, valves or flow channels[26]. The LC response shown in Fig. 4a–d can also prevent the release of excess agent (minimizing waste or toxicity) and extend the lifetime of the material so that it can withstand repeated triggering events (for example, releasing cleaning agents from a touch screen by exposure to physiological temperature). The optical response of the LC also permits self-reporting of the triggering event, which can be used to signal the amount of agent released and the remaining useful lifetime of the material.

We also used the results shown in Figs. 2 and 3 to design self-reporting and self-regulating LC materials that are triggered by mechanical shear stresses generated by the swimming motion of motile bacteria (for example, *Escherichia coli*). As noted above, interfacial shear stresses of 1 N m⁻² can reorient an LC (see Fig. 3 and associated text) and generate LC interfacial velocities v_x of 10 μm s⁻¹ (calculated from viscous stresses of about $\alpha(\partial v_x/\partial d)$ within the LC film, where α is the LC effective viscosity, $\alpha \approx 10^{-1}$ kg m⁻¹ s⁻¹). We observed that the arrival of motile bacterial cells moving at 30–40 μm s⁻¹ triggered shear-induced changes in the orientation of the LC, leading to optical reporting of the presence of bacteria (Fig. 4i) and triggering of the release of microcargo of antibacterial agents (Fig. 4e–h; Supplementary Video 3) via changes in F_{edl} and F_{e1} (see Fig. 3e, f). Non- ($v_x = 0$ μm s⁻¹) or weakly motile bacteria ($v_x < 10$ μm s⁻¹) generated insufficient shear stresses to trigger the LC (Extended Data Fig. 10). Whereas conventional controlled-release materials, used in areas such as healthcare, water purification and food safety, release active agents regardless of whether bacteria are present (which can lead to antibacterial resistance)[27] or not, our LC material designs are self-regulating; they do not release antibacterial agents in the absence of bacteria (Fig. 4f) and release only the minimum amount of biocidal agent required to kill the bacterial cells (Fig. 4g). Specifically, self-regulation involves a feedback loop in which the bacterial shear-triggered release of antibacterial agent causes cell death, which in turn eliminates the trigger and ends the release of antibacterial agent (Fig. 4h). In addition, the self-reporting function of the LC material signals the successful killing of the bacteria (Fig. 4i). To our knowledge, this is the first example of a material with the capability to provide a self-regulated release of chemoactive agents in response to mechanical forces generated by living cells.

Our results demonstrate that LC materials can be designed to report thermal, chemical and mechanical triggers and release microcargo in response to these triggers. Given the broad range of triggers and underlying colloidal interactions (for example, elastic, electrical double-layer and shear stresses) that are perturbed by these triggers, our results provide the basis for a highly versatile approach. For example, in addition to the results reported above, we have used LCs in free-standing forms, such as LC emulsion droplets (Extended Data Fig. 11). We have also designed LC systems that respond to combinations of stimuli (for example, thermal plus chemical), thus providing more selective responses than is possible with a single stimulus (Extended Data Fig. 11). We note that specific biological processes, including specific binding events[28] and interfacial enzymatic events[29], can lead to changes in interfacial charge, thus enabling the introduction of additional selectivity into
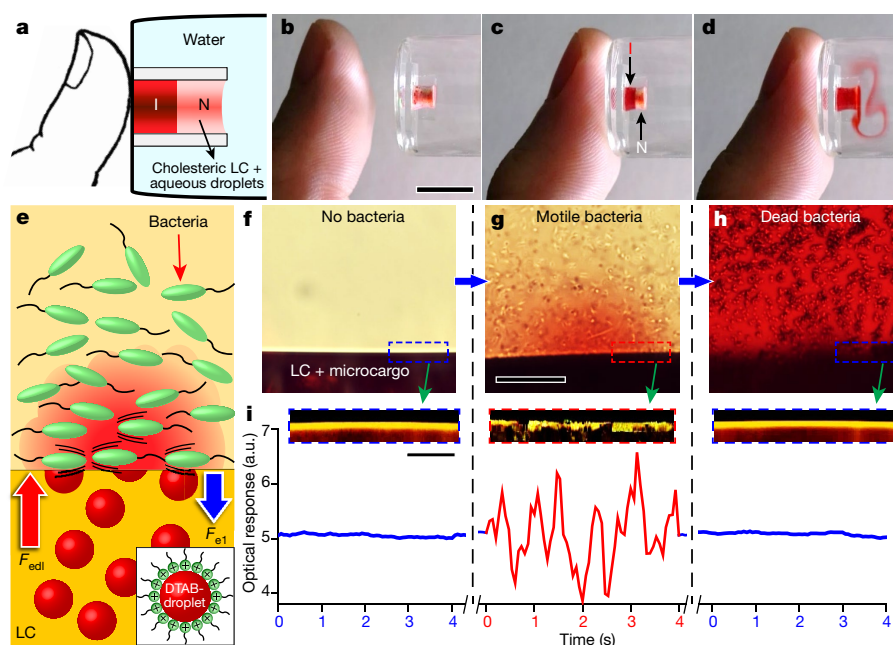
Fig. 4 | Release of microcargo from LCs by the heat of a human finger or by motile bacteria that generate interfacial shear stresses and interact with microcargo in a self-regulated manner. a–d, Schematic illustration (**a**) and sequential photographs (**b–d**) showing that the touch of a human finger can trigger a change in the Bragg diffraction of light and release of a well defined pulse of microdroplets ($C_{SDS} = 2$ mM and red tracer) from a cholesteric LC into the water (see Supplementary Video 2). Scale bar, 1 cm. **e–h**, Illustration (side view, **e**) and sequential photographs (side view, **f–h**) showing interfacial shear stresses generated by motile bacteria (10^7–10^8 *E. coli* cells per millilitre) triggering the self-regulated release of microdroplets containing anti-bacterial agent ($C_{DTAB} = 2$ mM and silver salts) and red tracer, before the arrival of bacteria (**f**), immediately after the arrival of motile bacteria (**g**; Supplementary Video 3) and two hours after the arrival of bacteria and following cell death (**h**). Scale bar, 40 μm. **i**, Optical responses and side views (crossed polars) of the LC interface corresponding to **f–h**. Scale bar, 10 μm.

the reporting and release of microcargo. Promising future directions include the use of magnetic or electric fields to modulate the responses and actions of LC systems, the use of other LC phases, such as smectic and edible lyotropic chromonic LCs[30] and the triggered release of solid microcargo from LCs (Extended Data Fig. 12).

Online content

Any Methods, including any statements of data availability and Nature Research reporting summaries, along with any additional references and Source Data files, are available in the online version of the paper at https://doi.org/10.1038/s41586-018-0098-y.

1. de Gennes, P. G. & Prost, J. *The Physics of Liquid Crystals* (Clarendon Press, Oxford, 1993).
2. Kleman, M. & Lavrentovich, O. D. *Soft Matter Physics: An Introduction* (Springer, New York, 2003).
3. Yang, D.-K. & Wu, S.-T. *Fundamentals of Liquid Crystal Devices* (John Wiley & Sons, Chichester, 2006).
4. Demus, D., Goodby, J., Gray, G. W., Spiess, H.-W. & Vill, V. *Handbook of Liquid Crystals* Vol. 2 (Wiley-VCH, New York, 1998).
5. Cuennet, J. G., Vasdekis, A. E., De Sio, L. & Psaltis, D. Optofluidic modulator based on peristaltic nematogen microflows. *Nat. Photon.* **5**, 234–238 (2011).
6. Bukusoglu, E., Pantoja, M. B., Mushenheim, P. C., Wang, X. & Abbott, N. L. Design of responsive and active (soft) materials using liquid crystals. *Annu. Rev. Chem. Biomol.* **7**, 163–196 (2016).
7. Lin, I. H. et al. Endotoxin-induced structural transformations in liquid crystalline droplets. *Science* **332**, 1297–1300 (2011).
8. Kim, Y.-K., Shiyanovskii, S. V. & Lavrentovich, O. D. Morphogenesis of defects and tactoids during isotropic nematic phase transition in self assembled lyotropic chromonic liquid crystals. *J. Phys. Condens. Matter* **25**, 404202 (2013).
9. Wood, T. A., Lintuvuori, J. S., Schofield, A. B., Marenduzzo, D. & Poon, W. C. K. A self-quenched defect glass in a colloid-nematic liquid crystal composite. *Science* **334**, 79–83 (2011).
10. Chernyshuk, S. B. & Lev, B. I. Theory of elastic interaction of colloidal particles in nematic liquid crystals near one wall and in the nematic cell. *Phys. Rev. E* **84**, 011707 (2011).
11. Pishnyak, O. P., Tang, S., Kelly, J. R., Shiyanovskii, S. V. & Lavrentovich, O. D. Levitation, lift, and bidirectional motion of colloidal particles in an electrically driven nematic liquid crystal. *Phys. Rev. Lett.* **99**, 127802 (2007).
12. Poulin, P., Stark, H., Lubensky, T. C. & Weitz, D. A. Novel colloidal interactions in anisotropic fluids. *Science* **275**, 1770–1773 (1997).
13. Loudet, J.-C., Barois, P. & Poulin, P. Colloidal ordering from phase separation in a liquid-crystalline continuous phase. *Nature* **407**, 611–613 (2000).
14. Musevic, I., Skarabot, M., Tkalec, U., Ravnik, M. & Zumer, S. Two-dimensional nematic colloidal crystals self-assembled by topological defects. *Science* **313**, 954–958 (2006).
15. Kim, Y.-K., Senyuk, B. & Lavrentovich, O. D. Molecular reorientation of a nematic liquid crystal by thermal expansion. *Nat. Commun.* **3**, 1133 (2012).
16. Mukherjee, P. K. The T_{NI}–T^* puzzle of the nematic-isotropic phase transition. *J. Phys. Condens. Matter* **10**, 9191–9205 (1998).
17. West, J. L. et al. Drag on particles in a nematic suspension by a moving nematic-isotropic interface. *Phys. Rev. E* **66**, 012702 (2002).
18. Loudet, J. C., Hanusse, P. & Poulin, P. Stokes drag on a sphere in a nematic liquid crystal. *Science* **306**, 1525 (2004).
19. White, T. J. & Broer, D. J. Programmable and adaptive mechanics with liquid crystal polymer networks and elastomers. *Nat. Mater.* **14**, 1087–1098 (2015).
20. Borshch, V. et al. Nematic twist-bend phase with nanoscale modulation of molecular orientation. *Nat. Commun.* **4**, 2635 (2013).
21. Mustin, B. & Stoeber, B. Single layer deposition of polystyrene particles onto planar polydimethylsiloxane substrates. *Langmuir* **32**, 88–101 (2016).
22. Zheng, Z. G. et al. Three-dimensional control of the helical axis of a chiral nematic liquid crystal by light. *Nature* **531**, 352–356 (2016).
23. Varney, M. C. M. et al. Periodic dynamics, localization metastability, and elastic interaction of colloidal particles with confining surfaces and helicoidal structure of cholesteric liquid crystals. *Phys. Rev. E* **90**, 062502 (2014).
24. Kearney, C. J. & Mooney, D. J. Macroscale delivery systems for molecular and cellular payloads. *Nat. Mater.* **12**, 1004–1017 (2013).
25. Zabara, A. & Mezzenga, R. Controlling molecular transport and sustained drug release in lipid-based liquid crystalline mesophases. *J. Control. Release* **188**, 31–43 (2014).
26. Nguyen, N.-T., Shaegh, S. A. M., Kashaninejad, N. & Phan, D.-T. Design, fabrication and characterization of drug delivery systems based on lab-on-a-chip technology. *Adv. Drug Deliv. Rev.* **65**, 1403–1419 (2013).
27. Lehar, S. M. et al. Novel antibody-antibiotic conjugate eliminates intracellular S. aureus. *Nature* **527**, 323–328 (2015).
28. Sidiq, S., Prasad, G., Mukhopadhaya, A. & Pal, S. K. Poly(L-lysine)-coated liquid crystal droplets for cell-based sensing applications. *J. Phys. Chem. B* **121**, 4247–4256 (2017).
29. Ma, C. D. et al. Liquid crystal interfaces programmed with enzyme-responsive polymers and surfactants. *Small* **11**, 5747–5751 (2015).
30. Lydon, J. Chromonic review. *J. Mater. Chem.* **20**, 10071–10099 (2010).

Author contributions The experimental strategy was proposed initially by N.L.A. and developed by all authors. Experiments were performed by Y.-K.K. with assistance from X.W., P.M. and E.B. and analysed by Y.-K.K. and N.L.A. Y.-K.K. and N.L.A. wrote the manuscript with input from all co-authors.

Competing interests The University of Wisconsin-Madison has filed a patent application (PCT/US207/037414) on the work described in this manuscript. The inventors listed on the patent application are N.L.A., Y.-K.K., X.W. and E.B.

Additional information
Extended data is available for this paper at https://doi.org/10.1038/s41586-018-0098-y.
Supplementary information is available for this paper at https://doi.org/10.1038/s41586-018-0098-y.
Reprints and permissions information is available at http://www.nature.com/reprints.
Correspondence and requests for materials should be addressed to N.L.A.
Publisher's note Springer Nature remains neutral with regard to jurisdictional claims in published maps and institutional affiliations.

METHODS

Comparison of the magnitudes of elastic and thermal energies. The elastic interaction energy E_e between a microdroplet and the boundaries of the nematic LC (for example, the interfaces of N–overlying aqueous phase, N–glass, N–I) can be written as[10–12]:

$$E_e = A^2 B \pi K \frac{R^4}{(h+R)^3} \qquad (1)$$

where A is a numerical factor ($A = 2.04$ for microdroplets of $R > K/W$ with homeotropic anchoring in an N phase and $A = 0$ for microdroplets of $R < K/W$ or in an I phase)[10], B is the anchoring-dependent constant ($B = 3/4$ and $B = 1/2$ for planar and homeotropic anchoring, respectively, at the boundaries of nematic LCs), R is the radius of the guest microdroplet, h is the distance between a microdroplet surface and the nematic boundary and $K = (K_1 + K_3)/2$ is the Frank elastic constant of the LC, where K_1 and K_3 are elastic constants for splay and bend deformations, respectively[1]. As a microdroplet approaches a nematic interface, E_e increases and exhibits a maximum at $h = 0$. Because $K \approx 10^{-12}$ N for typical thermotropic LCs, the maximum elastic interaction energy E_e^{max} for a microdroplet with $R = 1\,\mu m$ and $B = 3/4$ is 9.8×10^{-18} J. $k_B T = 4.1 \times 10^{-21}$ J at $T = 25\,°C$, and thus $E_e^{max} = 2{,}383 k_B T$.

Comparison of the magnitudes of elastic forces and buoyant forces. Based on equation (1), the elastic repulsive force F_e between a microdroplet and a nematic interface can be written as[10,11]

$$F_e \approx \pm A^2 B \pi K \left(\frac{R}{h+R} \right)^4 \qquad (2)$$

F_e is valid for a microdroplet in an N phase and needs to be modified for a microdroplet at an N–I interface (see below). The maximum F_e is $F_e^{max} = A^2 B \pi K$ at $h = 0$ and the buoyant force F_b acting on a microdroplet in the LC is $F_b = (4/3)\pi R^3 g(\rho_{LC} - \rho_{aq})$. At 25 °C, $K_{5CB} = 7.3$ pN (ref. [31]), $K_{E7} = 14.4$ pN (ref. [32]), $\rho_{5CB} = 1.010\,g\,cm^{-3}$ (ref. [33]), and we measured $\rho_{E7} = 1.057\,g\,cm^{-3}$, $\rho_{aq} = 1.018\,g\,cm^{-3}$ with red dye and $\rho_{aq} = 1.012\,g\,cm^{-3}$ with green dye. Therefore, for a microdroplet (red dye) of $R = 3\,\mu m$ and $B = 3/4$ in 5CB, we get $F_e^{max} = 8{,}072 F_b$ and for a microdroplet (green dye) of $R = 4\,\mu m$ and $B = 3/4$ in E7, we have $F_e^{max} = 1{,}194 F_b$.

Net force $F_h^{net}(z)$ upon heating (Fig. 1). The net force $F_h^{net}(z)$ acting on a quasi-static microdroplet with respect to the distance z between the centre of the microdroplet and the N–I interface ($z = 0$) upon heating can be written as

$$F_{h,N}^{net}(z) = \left[-A^2 B \pi K \left(\frac{R}{h_1+R} \right)^4 + A^2 B \pi K \left(\frac{R}{z} \right)^4 \right]_{F_{e1}}^{F_{e2}}$$
$$+ \left[\frac{4}{3}\pi R^3 g (\rho_{LC} - \rho_{aq}) \right]_{F_b} \qquad (3)$$

at $z \geq R$ (in the N phase; see Fig. 1l (i)),

$$F_{h,NI}^{net}(z) = \left[-A^2 B \pi K \frac{1}{\left(h_1 + \frac{z+R}{2}\right)^4} \left(\frac{z+R}{2} \right)^4 \right]_{F_{e1}} + \left[A^2 B \pi K \right]_{F_{e2}}$$
$$+ \left[\frac{4}{3}\pi R^3 g (\rho_{LC} - \rho_{aq}) \right]_{F_b} + \left[-2\pi R \sigma_{NI} \left(1 - \frac{z^2}{R^2} \right) \right]_{F_{it}}$$
$$+ \left[-\left(1 + \frac{z}{R} \right) \left\{ \alpha \left[WR + \frac{(WR)^2}{K} \right] + \beta K \right\} \right]_{F_{e*}} \qquad (4)$$

at $-R < z < R$ (at the N–I interface; see Fig. 1l (ii)), and

$$F_{h,I}^{net}(z) = \left[\frac{4}{3}\pi R^3 g (\rho_{LC} - \rho_{aq}) \right]_{F_b} \qquad (5)$$

at $z \leq -R$ (in the I phase; see Fig. 1l (iii)). In these equations, h_1 is the distance between the microdroplet surface and the interface between the LC and the overlying aqueous phase (Fig. 1a), $\alpha = 0$ for $R > K/W$, $A = \beta = 0$ for $R < K/W$, and $B = 3/4$ (parallel orientation at nematic boundaries).

When a microdroplet ($R > K/W$; homeotropic anchoring) is in the N phase ($z \geq R$), the net force $F_{h,N}^{net}(z)$ arises from F_b and F_e with[10,11] $A = 2.04$; see Fig. 1l (i). As the N–I interface ($z = 0$) approaches the microdroplet, $F_{h,N}^{net}(z)$ increases and becomes positive (upward) at $z < z^*$ (at $z = z^*$, $F_{h,N}^{net} = 0$) owing to the elastic

repulsion from the N–I interface (F_{e2} in equation (3)); $z^* = 17.0\,\mu m$ for a microdroplet with $R = 1.5\,\mu m$ and $h_1 = 1$ mm in 5CB. This reveals that the microdroplet will be levitated at $z = z^*$ above the N–I interface. $F_{h,N}^{net}(z)$ shows a maximum at $z = R$ (red curve in Fig. 1l).

When the microdroplet penetrates the N–I interface ($-R < z < R$; Fig. 1l (ii)), two additional forces are generated from the changes in interfacial tensions[17,34] (F_{it}) and elastic strain[17,35] (F_{e*}). These forces drive the microdroplets into the I phase (Fig. 1l (ii)); see separate sections on F_{it} and F_{e*} for additional detail. Additionally, F_e needs to be modified because the part of the microdroplet that protrudes into the I phase no longer strains the LC. Because R in equation (2) is the radius of a microdroplet in the N phase, for simplicity, we used $(R+z)/2$ for heating and $(R-z)/2$ for cooling as the effective radius of the part of each microdroplet in the N phase. We also need to take into account the decrease in the topological strength m of the microdroplet[2] from 1 to θ/π, where θ ($0 \leq \theta \leq \pi$) is half of the central angle of the part of the microdroplet in the N phase; see Extended Data Fig. 4a (ii). Because the elastic interaction is proportional[1,2] to m^2, the numerical factor A in equation (4) can be described as $A = 2.04\,m = (2.04/\pi)\cos^{-1}(-z/R)$. Consequently, $F_{h,NI}^{net}(z)$ decreases rapidly at $-R < z < R$ (blue curve in Fig. 1l).

When the microdroplet is in the I phase ($z \leq -R$; Fig. 1l (iii)), the net force $F_{h,I}^{net}(z)$ is composed of only F_b; $A = 0$ and thus $F_e = 0$. Therefore, the microdroplets in 5CB ($\rho_{5CB} < \rho_{aq}$) sink whereas the microdroplets in E7 ($\rho_{E7} > \rho_{aq}$) rise.

Upon heating, the elastic repulsion from the N–I interface promotes release of the microdroplets (F_{e2} in equation (3)). Therefore, the moving N–I interface can only transport microdroplets with $R > K/W$ in the nematic phase ($F_{e2} \neq 0$). The interface passes through the microdroplets with $R < K/W$ because $F_{e2} = 0$.

Net force $F_c^{net}(z)$ upon cooling (Fig. 1). The net force $F_c^{net}(z)$ acting on a quasi-static microdroplet with respect to z can be written as:

$$F_{c,I}^{net}(z) = \left[\frac{4}{3}\pi R^3 g (\rho_{LC} - \rho_{aq}) \right]_{F_b} \qquad (6)$$

at $z \geq R$ (in the I phase; Extended Data Fig. 4a (i)),

$$F_{c,NI}^{net}(z) = \left[A^2 B \pi K \frac{1}{\left(h_2 + \frac{R-z}{2}\right)^4} \left(\frac{R-z}{2} \right)^4 \right]_{F_{e3}} + \left[-A^2 B \pi K \right]_{F_{e2}}$$
$$+ \left[\frac{4}{3}\pi R^3 g (\rho_{LC} - \rho_{aq}) \right]_{F_b} + \left[2\pi R \sigma_{NI} \left(1 - \frac{z^2}{R^2} \right) \right]_{F_{it}}$$
$$+ \left[\left(1 - \frac{z}{R} \right) \left\{ \alpha \left[WR + \frac{(WR)^2}{K} \right] + \beta K \right\} \right]_{F_{e*}} \qquad (7)$$

at $-R < z < R$ (at the N–I interface; see Extended Data Fig. 4a (ii)), and

$$F_{c,N}^{net}(z) = \left[A^2 B \pi K \left(\frac{R}{h_2+R} \right)^4 \right]_{F_{e3}} + \left[-A^2 B \pi K \left(\frac{R}{z} \right)^4 \right]_{F_{e2}} + \left[\frac{4}{3}\pi R^3 g (\rho_{LC} - \rho_{aq}) \right]_{F_b} \qquad (8)$$

at $z \leq -R$ (in the N phase; see Extended Data Fig. 4a (iii)). In these equations, F_{e3} is the upward elastic repulsion from an LC–glass interface and h_2 is the distance between a microdroplet surface and the LC–glass interface (Extended Data Fig. 5k). For $R > K/W$, $A = (2.04/\pi)\cos^{-1}(z/R)$ in equation (7) and $A = 2.04$ in equation (8); for $R < K/W$, $A = 0$; $B = 3/4$. In the I phase ($z \geq R$; see Extended Data Fig. 4a (i)), aqueous microdroplets in 5CB sink because $\rho_{5CB} < \rho_{aq}$ (that is, $F_{c,I}^{net}(z) < 0$).

In contrast to heating, the two additional forces (F_{it} and F_{e*}) at $-R < z < R$ are directed upwards upon cooling (see Extended Data Fig. 4a (ii)); $F_{it} > 0$ and $F_{e*} > 0$. As a result, $F_{c,NI}^{net}(z)$ becomes positive and exhibits a maximum at $-R < z < R$ (Extended Data Fig. 4a). Importantly, upon cooling $F_{it} > 0$ and $F_{e*} > 0$, regardless of R. This indicates that the cooling N–I interface can transport the microdroplets with both $R > K/W$ and $R < K/W$ (Extended Data Fig. 4b), whereas upon heating the interface cannot transport the microdroplets with $R < K/W$ (because $F_e = 0$).

At $z \leq -R$ (N phase; see Extended Data Fig. 4a (iii)), the microdroplets with $R > K/W$ are sequestered in a nematic bulk whereas the microdroplets with $R < K/W$ sediment away from the N–I interface.

In Fig. 1c–i, v_{NI} upon both cooling and heating was $37 \pm 3\,\mu m\,s^{-1}$, for which our model predicts the dispensing of microdroplets with $K/W \leq R \leq 3\,\mu m$ upon heating and $0.6\,\mu m \leq R \leq 6\,\mu m$ upon cooling. This prediction is consistent with our observation that the amount of tracer released upon cooling was greater than that released upon heating (Fig. 1g).

Interfacial tension force, F_{it}. When a microdroplet is near an interface dividing two immiscible fluids (N and I phase in our case), F_{it} arises to minimize the surface tension energy[34]. Typically, microdroplets are stabilized at the interface between two immiscible fluids because the interface tensions are similar in magnitude to each other. In thermotropic LCs, however, the surface tension at the N–I interface (σ_{NI}) is much smaller than the surface tension at the interfaces between the aqueous solution and the N (σ_{aq-N}) or I (σ_{aq-I}) phases. In the case of 5CB, for example, at $T = 35\,^{\circ}\text{C}$, $\sigma_{aq-N} \approx 7 \times 10^{-3}\,\text{J}\,\text{m}^{-2}$, $\sigma_{aq-I} \approx 6 \times 10^{-3}\,\text{J}\,\text{m}^{-2}$ and $\sigma_{NI} \approx 10^{-5}\,\text{J}\,\text{m}^{-2}$ ($\sigma_{aq-N} > \sigma_{aq-I} \gg \sigma_{NI}$)[33,36]. As a result, the aqueous microdroplets at the N–I interface are expelled to the I phase[34]. For simplicity, we assume that F_{it} is active only when the microdroplet contacts the N–I interface; $F_{it} = 0$ at $|z| \geq R$.

Elastic force, F_{e*}. When a microdroplet penetrates the N–I interface ($-R < z < R$), the elastic force acting on the microdroplet is modified[17,35] by F_{e*}. Whereas F_e acts to keep microdroplets in the nematic phase, F_{e*} expels the microdroplets into the isotropic phase to minimize the elastic free energy. In the weak anchoring regime ($R < K/W$), F_{e*} originates from the anchoring of the director at the microdroplet surface and the director deformation in the bulk nematic phase, and can be written as

$$F_{e*}(R < K/W) = \left[WR\,f_1(z/R) \right]_{\text{surface}} + \left[\frac{(WR)^2}{K} f_1(z/R) \right]_{\text{bulk}} \quad (9)$$

where $f_1(z/R)$ is a dimensionless function of the penetration depth (z/R) of a microdroplet into an N phase[17,35].

In the strong anchoring regime ($R > K/W$), F_{e*} is given by

$$F_{e*}(R > K/W) = \left[K\,f_2(z/R) \right]_{\text{bulk}} \quad (10)$$

where $f_2(z/R)$ is also a dimensionless function[17,35]. Andrienko et al.[37] found that the force acting on a particle passing through an N–I interface is linearly proportional to the penetration depth z/R. In our evaluation, therefore, we simplified the dimensionless functions to $f_1(z/R) = \alpha(\mp 1 - z/R)$ and $f_2(z/R) = \beta(\mp 1 - z/R)$ where – and + denote N-to-I and I-to-N phase transitions, respectively.

Electrical double-layer interaction, F_{edl} (Figs. 2 and 3). F_{edl} can be calculated as

$$F_{edl} = -4\pi\varepsilon_0\varepsilon\frac{R}{\lambda}\left(\frac{k_B T}{e_c}\right)^2 Y_p Y_i e^{-h/\lambda} \quad (11)$$

where ε_0 is the vacuum permittivity, ε is the relative permittivity of the LC, e_c is the elementary charge, Y_p is the effective surface potential of the microdroplet, Y_i is the effective surface potential of the interface between the LCs and the overlying aqueous phase and λ is the Debye screening length[21]. λ, Y_p and Y_i can be written as

$$\lambda = \sqrt{\frac{\varepsilon_0\varepsilon k_B T}{2e_c^2 N_A I}} \qquad Y_p = \frac{8\tanh(D\zeta_p e_c/k_B T)}{1 + \sqrt{1 - \frac{2(R/\lambda)+1}{((R/\lambda)+1)^2}\tanh^2\left(\frac{D\zeta_p e_c}{k_B T}\right)}}$$

$$Y_i = 4\tanh\left(\frac{D\zeta_i e_c}{k_B T}\right) \quad (12)$$

where N_A is the Avogadro constant ($N_A = 6.02 \times 10^{23}\,\text{mol}^{-1}$), I is the ionic strength of the LC, D is a numerical factor and ζ_p and ζ_i are the zeta potentials at the microdroplet surface and LC interface, respectively. In our evaluation, we used D values between 1 and 2 and $I = 1.8 \times 10^{-5}\,\text{mol}\,\text{m}^{-3}$ (corresponding to $\lambda \approx 0.66\,\mu\text{m}$ at the LC interface with planar anchoring); $\lambda \approx 1.5\,\mu\text{m}$ in 5CB without added electrolyte[38]. The range of D values reflects the fact that the surface potential ($\sim|D\zeta|$) is typically greater than the corresponding zeta potential[39] ($|\zeta|$). We note that the exact value of D does not change the conclusions of our model. The value of D will influence the calculated radius of the microdroplets above which the kinetic barrier (F_{i*}^{net}) will prevent release of the microdroplets. Because equation (11) is valid at $h > \lambda$ and it tends to overpredict[21] F_{edl} at $h < \lambda$, we only evaluated F_{edl} at $h \geq \lambda$.

In Figs. 2 and 3, therefore, the net force F_i^{net} can be written as

$$F_i^{net} = \left[-4\pi\varepsilon_0\varepsilon\frac{R}{\lambda}\left(\frac{k_B T}{e_c}\right)^2 Y_p Y_i e^{-h_1/\lambda}\right]_{F_{edl}} + \left[-(2.04)^2 B\pi K\left(\frac{R}{h_1+R}\right)^4\right]_{F_{e1}} \quad (13)$$

As shown in Fig. 2a–c, microdroplets containing anionic SDS ($C_{SDS} = 9\,\text{mM}$) elastically sequestered in LCs can be ejected by an upward F_{edl} (> 0) induced by the addition of cationic DTAB ($C_{DTAB} = 10\,\text{mM}$) into an overlying phase; for a microdroplet of $R = 1.5\,\mu\text{m}$ in 5CB, $F_{edl} = 9.2\,\text{pN}$ and $F_{e1} = -6.2\,\text{pN}$ at $h_1 = 1\,\mu\text{m}$. As evidenced by the optical response shown in Fig. 2, SDS or DTAB causes an anchoring transition from a parallel to perpendicular orientation at the interface

between the LCs and the overlying aqueous phase. Because the anchoring transition involves the variation of B and ε (for the parallel orientation $B = 3/4$ and $\varepsilon = (\varepsilon_\perp + \varepsilon_\parallel)/2$, and for the perpendicular orientation $B = 1/2$ and $\varepsilon = \varepsilon_\parallel$), F_{edl} increases, whereas F_{e1} decreases. For 5CB, $\varepsilon_\perp = 6.7$ and $\varepsilon_\parallel = 19.7$ at $T = 25\,^{\circ}\text{C}$ and we used $\varepsilon = (\varepsilon_\perp + \varepsilon_\parallel)/2 = 13.2$ for the parallel orientation at the interface between the LC and the overlying aqueous phase because the microdroplet interface exhibits homeotropic anchoring.

Ejection of microdroplets upon the convection or the arrival of motile bacteria (Figs. 3 and 4f–h). In the system, the net force is also expressed by equation (13). Microdroplets with cationic DTAB ($C_{DTAB} = 2\,\text{mM}$) have an upward F_{edl} but are elastically sequestered because F_{edl} cannot overcome F_{e1} under planar anchoring at the interface between the LC and the overlying aqueous phase (solid lines in Fig. 3e, f); $\varepsilon = (\varepsilon_\perp + \varepsilon_\parallel)/2 = 13.2$, $B = 3/4$, $F_{edl} = 6.5\,\text{pN}$ and $F_{e1} = -9.3\,\text{pN}$ at $h_1 = 1\,\mu\text{m}$ for $R = 1.5\,\mu\text{m}$. The introduction of convection or of the motile bacteria in the overlying phase, however, generates a dynamic fluctuation of the director orientation at the LC interface (Figs. 3a–d and 4i), leading to changes in both F_{e1} and F_{edl}. If homeotropic anchoring is induced, for example, ε increases to 19.7 ($\varepsilon = \varepsilon_\parallel$, $F_{edl} = 9.9\,\text{pN}$) from 13.2 ($F_{edl} = 6.5\,\text{pN}$), while B decreases to 1/2 ($F_{e1} = -6.2\,\text{pN}$) from 3/4 ($F_{e1} = -9.3\,\text{pN}$). Consequently, an enhanced F_{edl} can override the reduced F_{e1}, enabling the ejection of microdroplets from the LC (dashed lines in Fig. 3e, f).

Continuous release of microdroplets through thermal tuning of the elastic properties of the LC (Extended Data Fig. 5). To illustrate this point, we used a nematic LC called E7, with $\rho_{E7} > \rho_{aq}$ and $T_{NI}^{E7} = 60\,^{\circ}\text{C}$. At 25 °C, aqueous microdroplets ($0.5\,\mu\text{m} \leq R \leq 4\,\mu\text{m}$) were elastically sequestered in E7 because $F_{e1}/F_b = 1{,}194$. Both thermal tuning of the elastic properties (at $T < T_{NI}$; Extended Data Figs. 5 and 7) and isothermal tuning of the elastic properties by partitioning solutes into the LC (Extended Data Fig. 6) led to continuous release of microdroplets sequestered in the LC into the overlying aqueous phase. By contrast, when exposed to the same thermal stimulus, 5CB showed pulsatile release of microdroplets (Extended Data Fig. 5e–i). The experiment and modelling revealed that release from E7 occurred when $|F_{e1}|$ decreased below $|F_b|$ (Extended Data Fig. 5k), which in turn depended on R, h and T (thermal) or C (solute). With E7 at $T = 59\,^{\circ}\text{C}$, we calculated this constraint to be satisfied for $R > 22\,\mu\text{m}$ (Extended Data Fig. 5l, m). Consistent with this prediction, we observed that individual LC microdroplets with $R < 10\,\mu\text{m}$ were not released. Large microdroplets with $R > 22\,\mu\text{m}$, or clusters of LC microdroplets formed through LC-mediated elastic interactions[10–14] with an effective radius of $R > 22\,\mu\text{m}$, were released (Extended Data Fig. 7).

The net force F_b^{net} acting on a guest microdroplet in a nematic phase comprises F_b and F_e (Extended Data Fig. 5k), and is calculated as

$$F_b^{net}(z) = \left[-A^2 B\pi K\left(\frac{R}{h_1+R}\right)^4\right]_{F_{e1}} + \left[A^2 B\pi K\left(\frac{R}{h_2+R}\right)^4\right]_{F_{e3}} + \left[\frac{4}{3}\pi R^3 g(\rho_{LC} - \rho_{aq})\right]_{F_b} \quad (14)$$

where $A = 2.04$ and $B = 3/4$. Here, the upward forces are F_b ($\rho_{E7} > \rho_{aq}$) and the elastic repulsion from the LC–glass interface (F_{e3}).

Parameters used in the calculations. For 5CB, at $T = 25\,^{\circ}\text{C}$ we used $K_{5CB} = 7.3\,\text{pN}$ (ref. [31]) and $\rho_{5CB} = 1.010\,\text{g}\,\text{cm}^{-3}$ (ref. [33]), and at $T = 35\,^{\circ}\text{C}$ ($=T_{NI}^{5CB}$) we used $K_{5CB} = 3\,\text{pN}$ (ref. [31]), $\rho_{5CB} = 1.000\,\text{g}\,\text{cm}^{-3}$ (ref. [33]), $W = 10^{-6}\,\text{J}\,\text{m}^{-2}$ (ref. [8]) and $\eta_{5CB} = 0.015\,\text{kg}\,\text{m}^{-1}\,\text{s}^{-1}$ (ref. [40]). The σ_{NI} value of 5CB is $1.5 \times 10^{-5}\,\text{J}\,\text{m}^{-2}$ (ref. [36]). In our calculation, however, we used $\sigma_{NI} = 1.5 \times 10^{-6}\,\text{J}\,\text{m}^{-2}$ because the surfactants added to the microdroplets reduce the surface tension[41–43]. For E7, we used $K_{E7} = 14.4\,\text{pN}$ (25 °C), 10.25 pN (40 °C), 7 pN (50 °C) and 2 pN (59 °C)[32], and we measured $\rho_{E7} = 1.057\,\text{g}\,\text{cm}^{-3}$ (25 °C), 1.045 g cm^{-3} (40 °C), 1.037 g cm^{-3} (50 °C) and 1.028 g cm^{-3} (59 °C). We chose α and β on the basis of the experimental results as $\alpha = 9.9$ and $\beta = 0$ for $R < K/W$ and $\alpha = 0$, $\beta = 4.4$ for $R > K/W$. We used $h_1 = h_2 = 1\,\text{mm}$ for Fig. 1l and Extended Data Fig. 4, and $h_1 + h_2 + 2R = 3.5\,\text{mm}$ (thickness of LC layer in mini-wells) for Extended Data Fig. 5. For red-dye microdroplets (Fig. 1l, m and Extended Data Fig. 4), we measured $\rho_{aq} = 1.018\,\text{g}\,\text{cm}^{-3}$ (25 °C) and 1.013 g cm^{-3} (35 °C). For green-dye microdroplets (Extended Data Fig. 5l, m), we measured $\rho_{aq} = 1.012\,\text{g}\,\text{cm}^{-3}$ (25 °C), 1.004 g cm^{-3} (40 °C), 0.996 g cm^{-3} (50 °C) and 0.987 g cm^{-3} (59 °C). In F_{edl} calculations, we used $\zeta = +108$ ($C_{DTAB} = 10\,\text{mM}$), $+90$ ($C_{DTAB} = 2\,\text{mM}$), -116 ($C_{SDS} = 9\,\text{mM}$), -108.5 ($C_{SDS} = 5\,\text{mM}$) and $-42.5\,\text{mV}$ (no surfactants).

Materials. Nematic liquid crystals, 5CB and E7, and the chiral dopant S-811 were purchased from HCCH (Jiangsu Hecheng Display Technology Co., Ltd). Water-soluble dyes that were used as tracers were purchased from MontBlanc. SDS, DTAB, dimethyloctadecyl[3-(trimethoxysilyl)propyl]ammonium chloride (DMOAP), FITC-dextran, silver acetate and lipopolysaccharides (LPS) were purchased form Sigma-Aldrich. Lysogeny broth was purchased from Becton,

Dickinson and Company. Transmission electron microscopy (TEM) grids were purchased from Electron Microscopy Sciences. The polymeric alignment layer (PI2555) was purchased from HD Microsystems. A Sylgard 184 silicone elastomer kit for preparing polydimethylsiloxane (PDMS) was purchased from Dow Corning. Biopsy punches were obtained from Integra Miltex.

Preparation of LCs containing aqueous microdroplets. To stabilize the dispersions of aqueous microdroplets in the LCs, we first added either SDS or DTAB at a specified concentration to the aqueous solutions of water-soluble dyes (10 wt% with respect to aqueous solution). The aqueous solutions of dyes were emulsified into the nematic LCs (5CB or E7) by vortexing for 1 min at 3,000 revolutions per minute (r.p.m.) and sonication for 10 min. The volume fractions (v%) of aqueous microdroplets (C_{aq}) dispersed in the LCs were 20 v% for Figs. 1c–h and 2g ($C_{SDS} = 9$ mM), 0.5 v% for Fig. 1j–k ($C_{SDS} = 9$ mM), 5 v% for Fig. 2a–c ($C_{SDS} = 9$ mM), 10 v% for Fig. 3g, h and 4f–h ($C_{DTAB} = 2$ mM) and 10 v% for Fig. 4b–d ($C_{SDS} = 2$ mM). Each surfactant was present at a concentration below its critical micelle concentration.

Preparation of LC-filled mini-wells. Mini-wells were made of PDMS. Elastomer base and curing agent from a Sylgard elastomer kit were mixed in a ratio of 10:1. The mixture was then cured at 60 °C for 2 h. A cured PDMS disk with a diameter of 6 mm was obtained using a 6-mm biopsy punch. Subsequently, a cylindrical hole with a diameter of 3 mm was punched at the centre of the 6-mm-diameter disk using a second biopsy punch. The PDMS was treated with an oxygen plasma for 20 s and bonded to a glass substrate to create a mini-well with a depth of 3.5 mm. After fabrication, the mini-wells were stored for at least 3 days before filling with 18 μl of LCs containing guest microdroplets. Subsequently, the mini-wells were submerged into glass vials filled with 2 ml of aqueous solutions. If used within 3 days, the PDMS surface was sufficiently hydrophilic to allow water to spread between the LC phase and the PDMS surface.

Preparation of samples for microscopic observations. Experimental cells for microscopic observations were assembled from glass plates coated with a polyimide film (PI2555; Fig. 1j, k and Extended Data Fig. 2) or DMOAP (Fig. 4f–h and Extended Data Figs. 9b–e and 10), which caused planar and homeotropic alignment, respectively. PI2555 substrates were rubbed to achieve unidirectional alignment of n and were assembled in an anti-parallel fashion. The gaps (100–300 μm) between the plates were set by using double-sided tape. PI2555 cells were filled with the LCs containing microdroplets and then observed while either heating or cooling one edge of the optical cell to drive the N–I interface across the field of view. DMOAP cells were filled with aqueous solutions, followed by the LCs, and were then characterized using microscopy.

Preparation of LC films. As described in Figs. 2a–c and 3a–d (and Extended Data Figs. 3, 9f–i, 12), TEM grids were placed onto DMOAP-coated glass substrates and filled with LC containing the aqueous microdroplets. Subsequently, the films (40 μm in thickness) were submerged into aqueous baths. The DMOAP-coated glass was used to orient the LC perpendicular to the glass substrate and prevent penetration of the aqueous phase between the LC and the glass substrate.

Preparation of interfacial shear stresses (Fig. 3a–d, g and h). As shown in Figs. 3a–d, the LC films were submerged into aqueous SDS ($C_{SDS} = 2$ mM; homeotropic anchoring at LC–aqueous interface, Fig. 3a) and pure water (planar anchoring at LC–aqueous interface, Fig. 3c). Subsequently, shear stresses were induced at the interface between the LC and the bulk aqueous phase by circulating the latter with a pipette. Figure 3g and h shows a mini-well filled with 5CB containing microdroplets being submerged into a water bath. Subsequently, shear stresses were induced at the interface between the LCs and the bulk aqueous phase by rotating a magnetic bar (700–800 r.p.m.).

Preparation of cholesteric LC (Fig. 4a–d). 20 wt% of chiral dopant (S-811) was dissolved in 5CB. The clearing temperature of the LC was measured to be $T_{NI} = 27$ °C.

Preparation of bacterial dispersions (Fig. 4f–h). *Escherichia coli* (strain MG1655) were grown aerobically in 1 ml of lysogeny broth [1% (w/v) tryptone, 0.5% (w/v) yeast extract and 1% (w/v) NaCl] at temperature $T = 37$ °C with agitation (200 r.p.m.) for 12 h. To achieve motile bacteria, the culture was diluted into 2 ml of fresh lysogeny broth in a 1:100 ratio and the bacteria were grown again for 2 h ($T = 37$ °C, 200 r.p.m.). The density of bacteria in the resulting dispersion was 10^7–10^8 cells ml^{-1}.

Optical responses in Figs. 1e and 4i. The optical response shown in Fig. 1e is the intensity measured from the micrographs of mini-wells between crossed polarizers (insets in Fig. 1e). For the optical response in Fig. 4i, the transmittance at the LC–aqueous interface was averaged for every frame and the average values are plotted for 4 s for each sequence (Fig. 4f–h).

LC system with multiple stimuli (Extended Data Fig. 11). In this system, the mechanisms leading to the release of microcargo are the same as those described in Fig. 1 (thermal stimulus) and 2 (chemical stimulus). Specifically, the net force acting on microdroplets in the LC is described by $F_{edl} + F_{h,N}^{net}$ (see equations (3) and

(11)) during heating and $F_{edl} + F_{c,NI}^{net}$ (see equation (7)) during cooling. Because the sign and amplitude of F_{edl} can be manipulated by charged surfactants added into overlying aqueous phases, we predicted that the combination of thermal and chemical stimuli would enable selective release of two agents that are oppositely charged. To test this prediction, Wells 1 and 2 were filled with 5CB containing microdroplets ($C_{aq} = 20$ v%) doped with DTAB ($C_{DTAB} = 9$ mM, $\zeta > 0$, and green tracer) and SDS ($C_{SDS} = 9$ mM, $\zeta < 0$, and red tracer), respectively, and then were submerged into an aqueous SDS solution (3 mM, $\zeta < 0$). Under these conditions, $F_{edl} > 0$ in Well 1 ($\zeta < 0$ at the interface between the LCs and the overlying aqueous phase, but $\zeta > 0$ at their interface with the microdroplets), while $F_{edl} < 0$ in Well 2 ($\zeta < 0$ at both interfaces). Upon thermally triggering phase transitions (0th to 4th phase transitions, $T_h = 50$ °C and $T_c = 25$ °C), Well 1 released green tracer owing to the attractive F_{edl} and the elastic forces (F_{e2} for heating, equation (3); elastic strain F_{e*} and interfacial tension F_{it} forces for cooling, equation (7)) generated by the motion of the N–I interface. By contrast, no release was observed from Well 2 because the attractive elastic forces did not override the repulsive F_{edl}. After four phase transitions, aqueous DTAB ($C_{DTAB} = 3$ mM) was introduced into the bath to reverse the charge at the interface between the LCs and the overlying aqueous phase from $\zeta < 0$ to $\zeta > 0$ (and thus $F_{edl} < 0$ in Well 1 and $F_{edl} > 0$ in Well 2). Consequently, the elastic forces were able to trigger the release of microcargo from Well 2 ($F_{edl} > 0$, red tracer) but not Well 1 ($F_{edl} < 0$, green tracer).

Temperature control. The temperature was controlled using a STC200 hot stage and a controller (Instec Inc.) with and accuracy of 0.1 °C. Both heating and cooling were achieved by circulation of cold water. The rate of temperature change was typically ± 15 °C min^{-1}.

Measurement for the mass of tracer released. 6 μl of aqueous solution was collected from the baths contacting the LCs after each N–I phase transition (Fig. 1 and Extended Data Fig. 1i and 11f) or every 2–5 min (Fig. 2g and Extended Data Fig. 5j). Prior to collection of a sample, the baths were gently agitated to uniformly mix the tracer released from the LCs through the overlying aqueous solution. We estimated the mass of tracer released from the absorbance of the samples at a wavelength corresponding to peak tracer absorbance, which was measured using a NanoDrop 2000 (Thermo Scientific) spectrophotometer.

Zeta potential measurement. 5CB (0.01 v% $\geq C_{5CB} \geq 0.001$ v%) was emulsified in aqueous solution (water or aqueous solutions of SDS or DTAB) using a homogenizer. The zeta potentials on the aqueous side of the LC–aqueous interface were measured using a Zetasizer Nano instrument (Malvern Instruments Ltd).

Additional observations on the transport of microdroplets by propagating N–I interfaces. We made two additional observations in the experiments shown in Fig. 1j, k and Extended Data Fig. 2. First, we observed single microdroplets or microdroplet clusters with $R < R^*$ to be transported initially by the moving N–I interface (denoted by dotted circles in Extended Data Fig. 2c, d, g and h). However, as the moving interface formed bigger clusters with $R > R^*$ by collecting additional microdroplets, we observed some microdroplets from the cluster to be left behind the interface, as illustrated in Extended Data Fig. 2i–l. West et al.[17] observed similar behaviours with solid particles and attributed them to an increase in the effective radius of the particles due to aggregation. Importantly, this observation provides insight into why only a fraction of the microdroplets was released at each phase transition (Fig. 1g).

Second, we observed microdroplets to occasionally coalesce upon heating (denoted by white arrows in Extended Data Fig. 2c, d). Consequently, large microdroplets formed, which were observed to remain behind the moving N–I interface. This latter observation provides insight into why the amount of tracer released after 20 cycles corresponded to approximately 40% of the tracer loaded initially into the 5CB (Fig. 1i). Overall, these results indicate that the fraction of microdroplets released can be manipulated by tuning the clustering size and coalescence of microdroplets.

Data availability. The authors declare that the main data supporting the findings of this study are available within the paper and in Supplementary Information. Additional data are available from the corresponding author upon reasonable request.

31. Bogi, A. & Faetti, S. Elastic, dielectric and optical constants of 4′-pentyl-4-cyanobiphenyl. *Liq. Cryst.* **28**, 729–739 (2001).
32. Raynes, E. P., Tough, R. J. A. & Davies, K. A. Voltage dependence of the capacitance of a twisted nematic liquid crystal layer. *Mol. Cryst. Liq. Cryst.* **56**, 63–68 (1979).
33. Kim, J.-W., Kim, H., Lee, M. & Magda, J. J. Interfacial tension of a nematic liquid crystal/water interface with homeotropic surface alignment. *Langmuir* **20**, 8110–8113 (2004).
34. Israelachvili, J. N. *Intermolecular and Surface Forces* 3rd edn (Elsevier Science, Burlington, 2010).
35. Zimmermann, N., Junnemann-Held, G., Collings, P. J. & Kitzerow, H.-S. Self-organized assemblies of colloidal particles obtained from an aligned chromonic liquid crystal dispersion. *Soft Matter* **11**, 1547–1553 (2015).

36. Faetti, S. & Palleschi, V. Measurements of the interfacial tension between nematic and isotropic phase of some cyanobiphenyls. *J. Chem. Phys.* **81**, 6254–6258 (1984).
37. Andrienko, D., Tasinkevych, M., Patricio, P. & da Gama, M. M. T. Interaction of colloids with a nematic-isotropic interface. *Phys. Rev. E* **69**, 021706 (2004).
38. Shah, R. R. & Abbott, N. L. Coupling of the orientations of liquid crystals to electrical double layers formed by the dissociation of surface-immobilized salts. *J. Phys. Chem. B* **105**, 4936–4950 (2001).
39. Brown, M. A. et al. Determination of surface potential and electrical double-layer structure at the aqueous electrolyte-nanoparticle interface. *Phys. Rev. X* **6**, 011007 (2016).
40. Janik, J., Krol-Otwinowska, A., Sokolowska, D. & Moscicki, J. K. Pendulum viscometer: a new method for measurement of Miesowicz nematic shear viscosity coefficients η_1 and η_2. *Rev. Sci. Instrum.* **77**, 123906 (2006).
41. Holmberg, K., Jönsson, B., Kronberg, B. & Lindman, B. *Surfactants and Polymer in Aqueous Solution* (John Wiley & Sons, Chichester, 2002).
42. Harth, K., Shepherd, L. M., Honaker, J. & Stannarius, R. Dynamic interface tension of a smectic liquid crystal in anionic surfactant solutions. *Phys. Chem. Chem. Phys.* **17**, 26198–26206 (2015).
43. Ong, L. H. & Yang, K.-L. Surfactant-driven assembly of poly(ethylenimine)-coated microparticles at the liquid crystal/water interface. *J. Phys. Chem. B* **120**, 825–833 (2016).
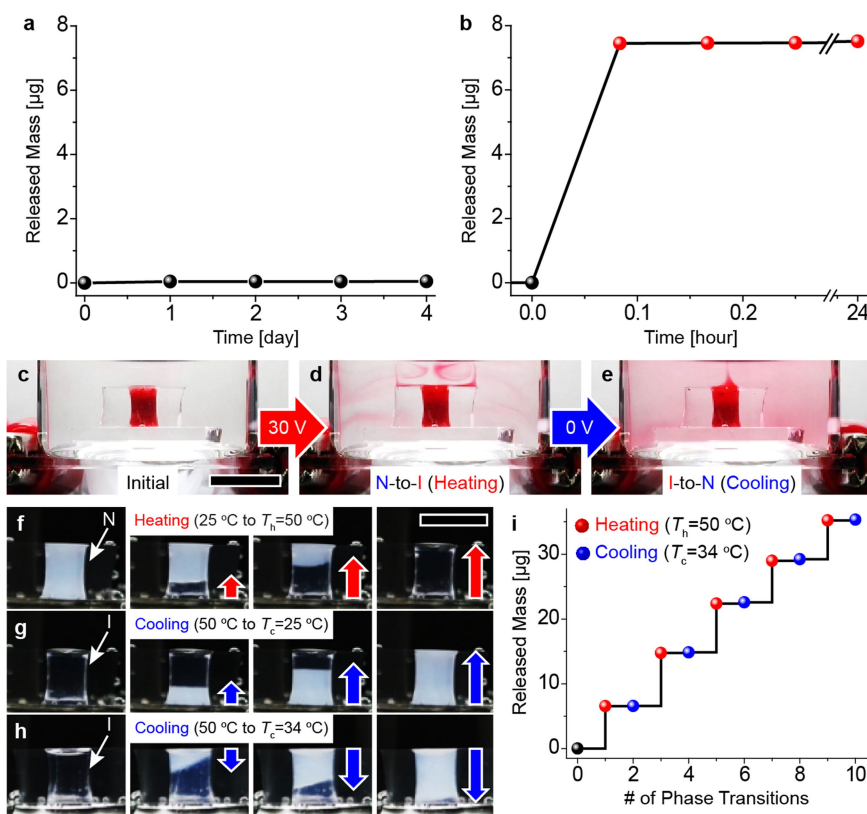
Extended Data Fig. 1 | Thermally triggered ejection of microdroplets. **a**, **b**, Mass of tracer released from LCs (5CB) as a function of time, before (**a**) and after (**b**) an N-to-I phase transition (corresponds to Fig. 1). Black and red points indicate the mass released before and after an N–I phase transition, respectively. **c–e**, Sequential photographs of the release of microdroplets ($C_{SDS} = 9$ mM and red tracer) from the LC, which is triggered by phase transitions induced by resistive heating. We used $C_{aq} = 20$ v% and 30 V for heating (to $T_h = 60\,^{\circ}$C, **d**) and 0 V for cooling (to room temperature, **e**). Heating of the sample from below was achieved by passing a current through an indium-tin-oxide electrode coated on glass. The motion of the N–I interface was upward for both heating and cooling. **f–h**, Dependence of the direction of motion of the N–I interface on T_h and T_c. **f**, Optical images showing a propagation of the N–I interface across a mini-well filled with 5CB (containing no microdroplets) in an aqueous bath upon heating from $T = 25\,^{\circ}$C to $T_h = 50\,^{\circ}$C (N-to-I phase transition). Upon heating the sample from below, the interface moved upwards (towards the interface between the LCs and the overlying aqueous phase) regardless of T_h. **g**, Upward motion of the N–I interface upon cooling from $T = 50\,^{\circ}$C to $T_c = 25\,^{\circ}$C (I-to-N phase transition). **h**, Downward motion of the N–I interface upon cooling from $T = 50\,^{\circ}$C to $T_c = 34\,^{\circ}$C (I-to-N phase transition). Scale bars, 5 mm. **i**, Released mass of tracer as a function of the number of phase transitions with $T_h = 50\,^{\circ}$C and $T_c = 34\,^{\circ}$C; $C_{aq} = 20$ v% ($C_{SDS} = 9$ mM).
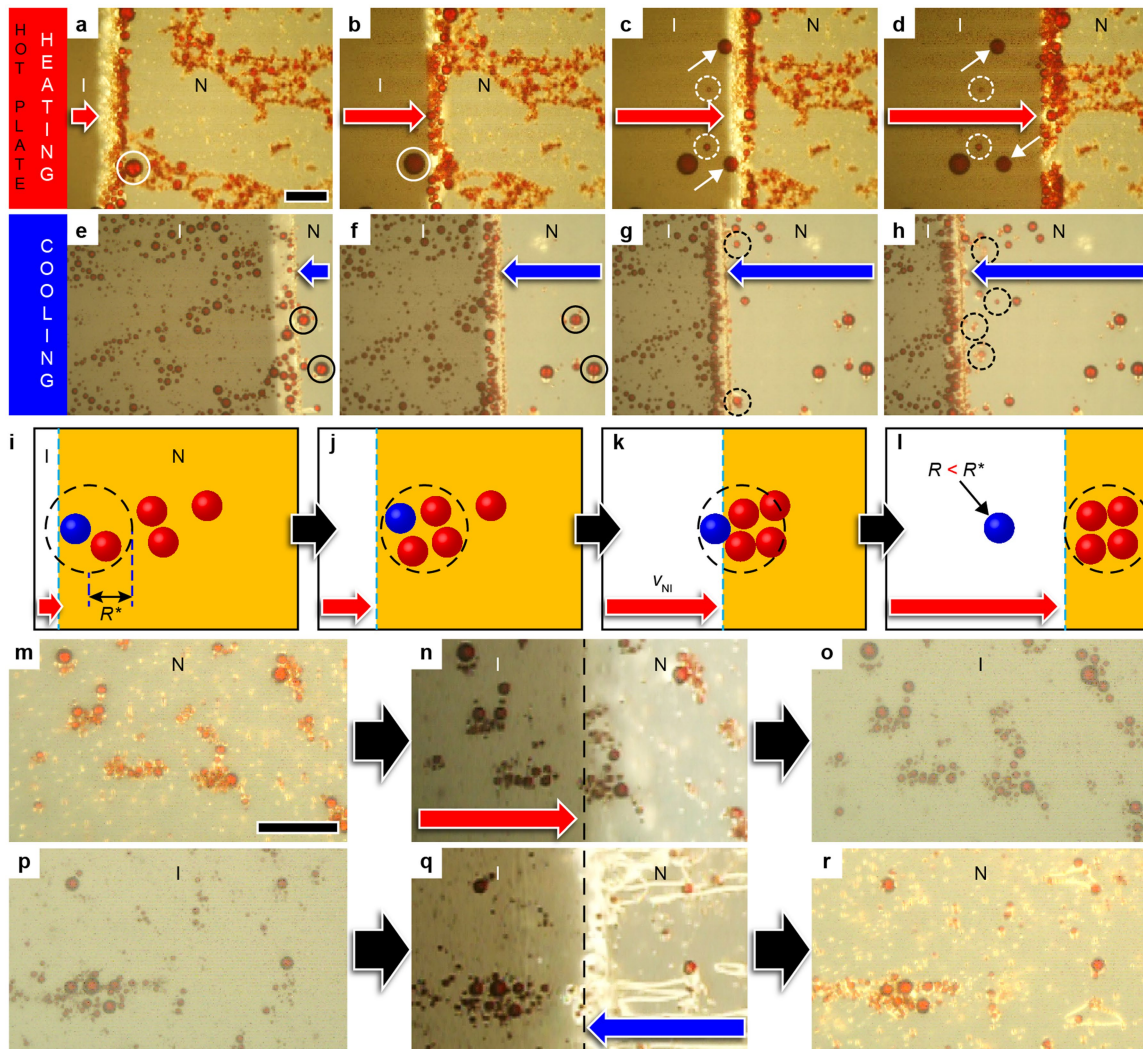
Extended Data Fig. 2 | Behaviours of microdroplet clusters during passage of the N–I interface. a–h, Sequential micrographs showing the behaviours of microdroplet clusters dispersed in an LC (5CB) during passage of an N–I interface upon an N-to-I (heating, **a–d**) and an I-to-N (cooling, **e–h**) phase transition. We used $C_{aq} = 3$ v% ($C_{SDS} = 2$ mM) and measured $v_{NI} = 10\,\mu$m s^{-1} for heating, $v_{NI} = 35\,\mu$m s^{-1} for cooling and $R^* \approx 10\,\mu$m for both cases. Scale bar, $100\,\mu$m (see Methods, 'Additional observations on the transport of microdroplets by propagating N–I interfaces' for more details). Red and blue arrows indicate the direction of motion of the N–I interface. Solid and dotted circles indicate microdroplets with $R > R^*$ ($= 10\,\mu$m) and $R < R^*$, respectively. White arrows indicate microdroplets that coalesced while being transported by the moving N–I interface. We note that microdroplets with $R < R^*$ were left behind the N–I interface in **c** because they were shed from clusters, as illustrated in **i–l**. **i–l**, Illustration of a microdroplet cluster being transported by a moving N–I interface. **i**, Single microdroplets or microdroplet clusters with $R < R^*$ are transported by a moving N–I interface. **j**, As the moving interface collects more microdroplets, the microdroplet clusters formed at the interface increase in size. **k**, When the effective radius of a microdroplet cluster exceeds R^*, the interface no longer transports the cluster. **l**, Because some of microdroplets from the cluster are left behind the N–I interface, the cluster becomes smaller than R^* and thus is transported again by the interface. **m–r**, Evidence that microdroplets with $R > R^*$ are not transported by an N–I interface moving at high speed ($v_{NI} = 100\,\mu$m s^{-1}) during N-to-I (**m–o**) and I-to-N (**p–r**) phase transitions. Here $C_{aq} = 0.5$ v% and $C_{SDS} = 2$ mM. Scale bar, $100\,\mu$m. The left (**m**, **p**) and right (**o**, **r**) columns show optical micrographs before and after passage of the N–I interface, respectively, and the middle column (**n**, **q**) shows micrographs taken during passage of the N–I interface. The positions of microdroplets before and after the passage of the N–I interface were unchanged, revealing that $R > R^*$ for the rapidly moving interface.
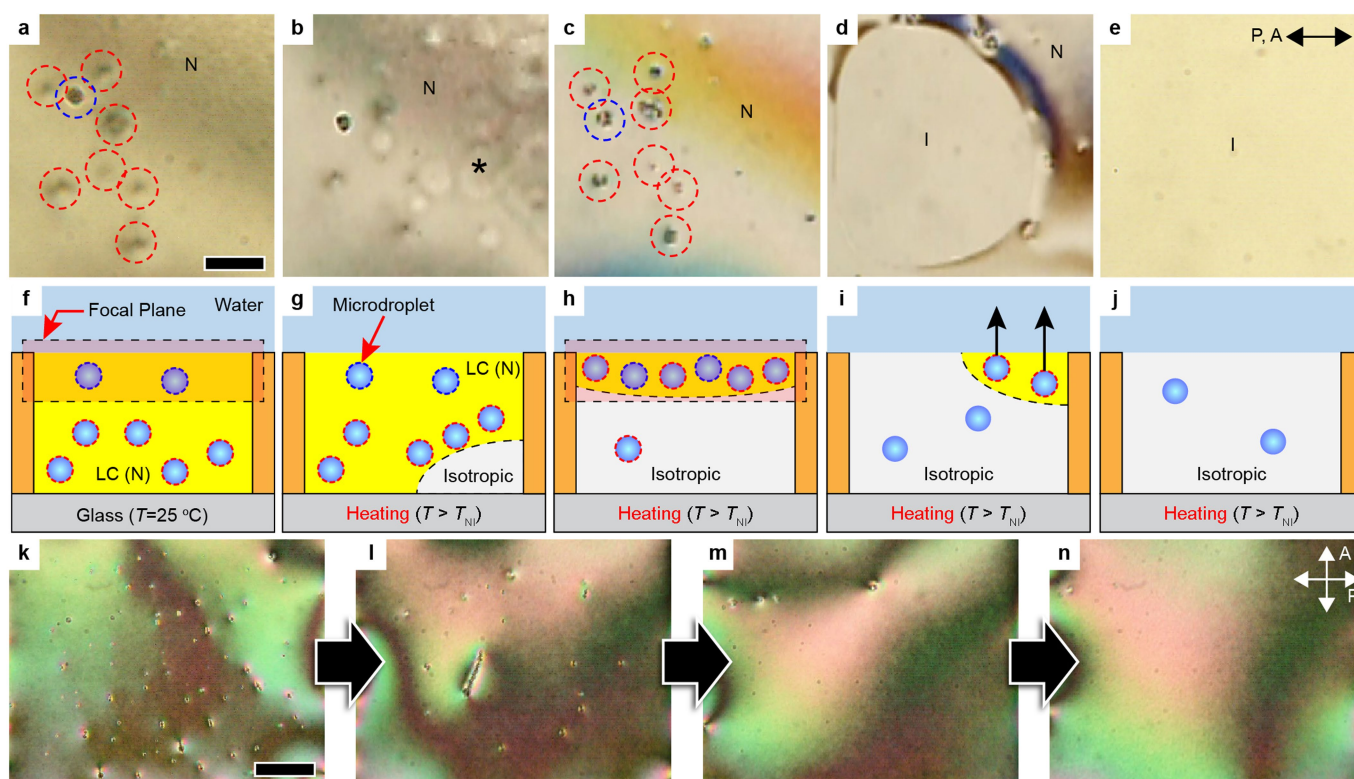
Extended Data Fig. 3 | Transport of microdroplets by an N–I interface propagating across an LC film. a–j, Sequential micrographs (**a–e**, top view) and corresponding illustrations (**f–j**, side view) of microdroplets transported by a moving N–I interface upon heating in an LC film (5CB, 40 μm in thickness). The focal plane is near the interface between the LC and the overlying water (red boxes in **f** and **h**). **a, f**, Microdroplets are dispersed initially in the LC bulk. **b, g**, When the bottom of the LC film is heated to $T_h = 50\,°C$ ($> T_{NI}$), the N-to-I transition first occurs at the LC–glass interface (denoted by the asterisk in **b**) and the N–I interface propagates upwards, towards the LC–water interface. **c, h**, Microdroplets that were out of focus (red dashed circles in **a** and **f**) move into focus, revealing that the moving interface transported the microdroplets towards the LC–water interface. **d, i**, As the N–I interface reaches the LC–water interface, the microdroplets disappear, consistent with their fusion with the overlying aqueous phase. **e, j**, After the phase transition, some microdroplets remain in the LC layer. **k–n**, Micrographs showing the decrease in the population of microdroplets in the LC at $T = 25\,°C$; before any phase transitions (**k**) and after 2 (**l**), 4 (**m**) and 6 (**n**) phase transitions. Scale bars, 50 μm. P and A indicate the orientations of the polarizer and analyser, respectively. $T_h = 50\,°C$, $T_c = 25\,°C$, $C_{aq} = 5\,vol\%$ ($C_{SDS} = 9\,mM$) and $\nu_{NI} = 8\,\mu m\,s^{-1}$.
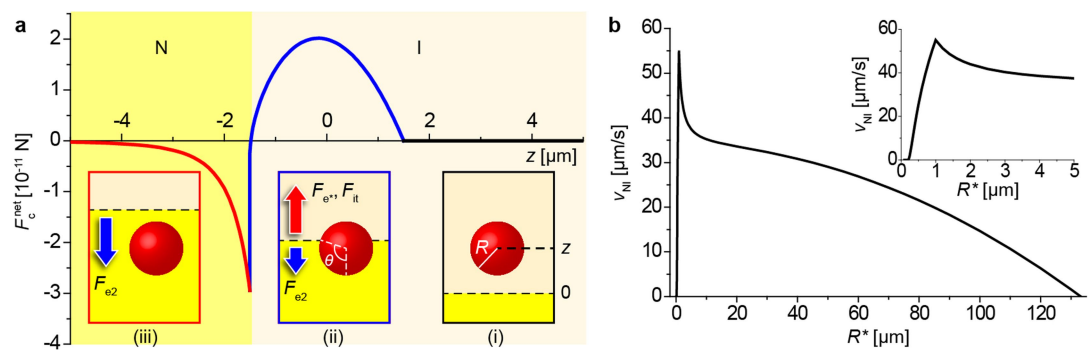
Extended Data Fig. 4 | Calculated net force $F_c^{net}(z)$ acting on a microdroplet and calculated dependence of R^* on v_{NI} during an I-to-N phase transition (cooling). a, $F_c^{net}(z)$ for a quasi-static microdroplet of $R = 1.5\,\mu m$ in 5CB. The insets show microdroplets at $z \geq R$ (black line; (i)), at $-R < z < R$ (blue line; (ii)) and at $z \leq -R$ (red line; (iii)). **b**, Critical radius R^* of a microdroplet as a function of v_{NI} upon cooling. See Methods for details.
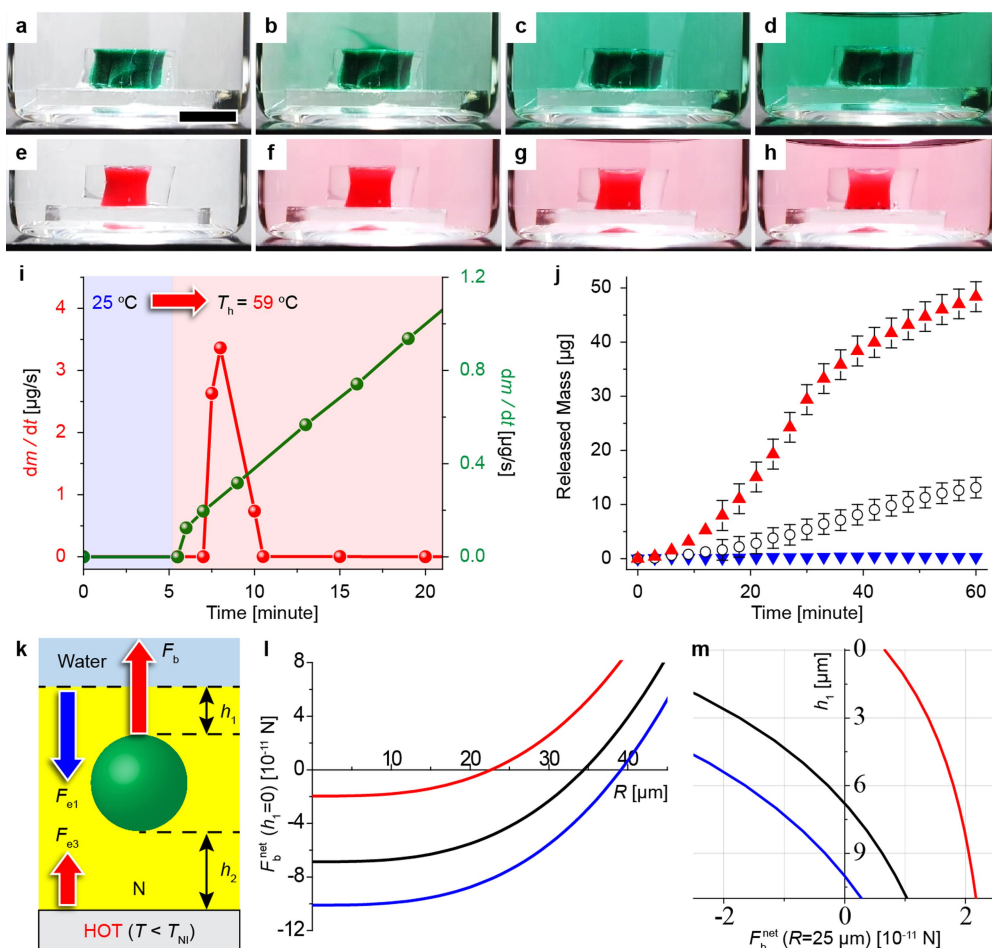
Extended Data Fig. 5 | Influence of LC phase behaviour and elastic properties on dynamics of release of dispersed microdroplets.
a–h, Sequential photographs showing continuous release (a–d) of dispersed microdroplets (green tracer and $C_{SDS} = 2$ mM) from a nematic LC (E7) in response to a thermal trigger $T_h < T_{NI}^{5CB}$ ($\rho_{E7} > \rho_{aq}$), and for pulsatile release of dispersed microdroplets (red tracer and $C_{SDS} = 9$ mM) from 5CB ($\rho_{5CB} < \rho_{aq}$, $T_h > T_{NI}^{5CB}$) at 0 min (a, e), 15 min (b, f), 60 min (c, g) and 120 min (d, h) after heating of the baths from below to $T_h = 59$ °C. We used $C_{aq} = 30$ v% for a–d and $C_{aq} = 20$ v% for e–h. Scale bar, 5 mm. i, Corresponding time derivative of the released mass m of the tracer (dm/dt; t, time) for pulsatile (red line and circles) and continuous (green line and circles) release. j, Released mass of green tracers from E7 (continuous release) with respect to time at representative temperatures of $T = 40$ °C (blue triangles), 50 °C (circles) and 59 °C (red triangles). The data are mean values and the error bars are 1 s.d. ($n = 5$). k, Forces acting on an aqueous microdroplet in E7. l, m, Calculated net force F_b^{net} acting on a microdroplet in E7 as a function of R at $h_1 = 0$ (l) and as a function of h_1 for $R = 25$ μm (m) at $T = 40$ °C (blue line), 50 °C (black line) and 59 °C (red line). See Methods for details.
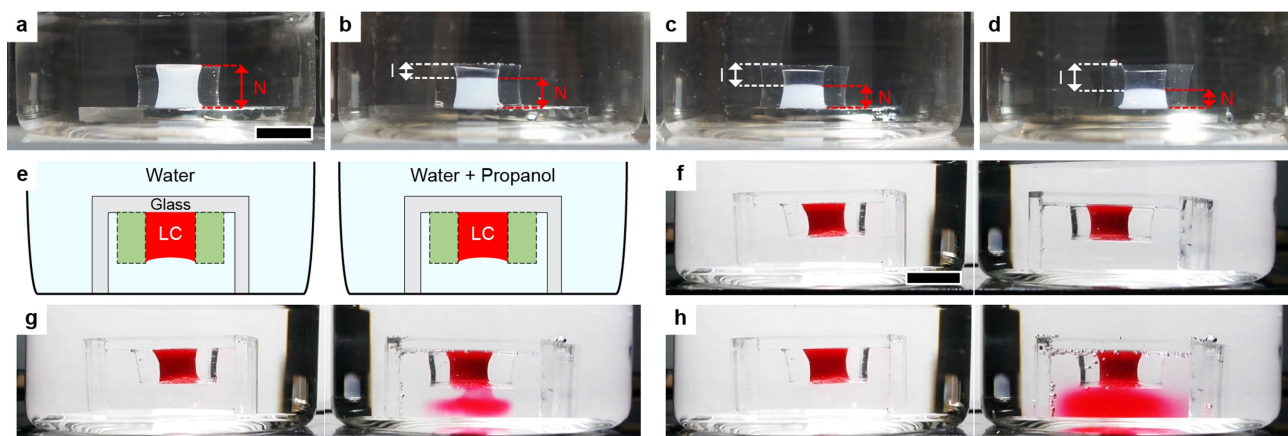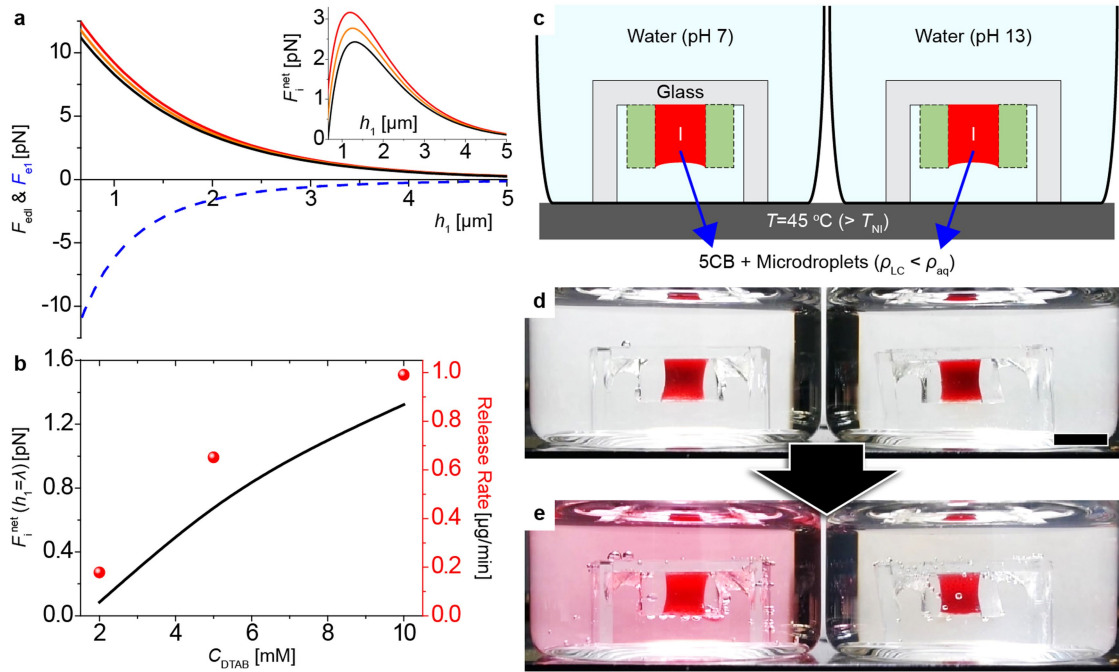
Extended Data Fig. 6 | Isothermal release of microdroplets from an LC by a solute-triggered N-to-I phase transition. a–d, Sequential photographs of a solute-triggered N-to-I phase transition of 5CB at $T = 25\,°C$ ($T_{NI}^{5CB} = 35\,°C$) at 0 h (**a**), 1 h (**b**), 2 h (**c**) and 3 h (**d**) after the addition of propanol to the overlying water. As the propanol diffused into the 5CB, an N-to-I transition occurred first at the interface between the LC and the aqueous solution and propagated into the LC bulk. **e,** Illustration of inverted mini-wells filled with 5CB containing microdroplets (red tracer), placed in baths containing pure water (left) and water containing propanol ($C_{propanol} = 16\,v\%$; right). **f–h,** Sequential photographs of the mini-wells at 0 min (**f**), 5 min (**g**) and 30 min (**h**) after the mini-wells were submerged into the baths; $C_{aq} = 10\,v\%$ ($C_{SDS} = 9\,mM$). Although F_b ($\rho_{LC} < \rho_{aq}$) promotes the release of tracers, no release of red tracers was observed in the left bath owing to strong elastic sequestration. In the right bath, however, the red tracers were continuously released as the elastic barrier was removed by the solute-induced N-to-I phase transition. Scale bars, 5 mm.
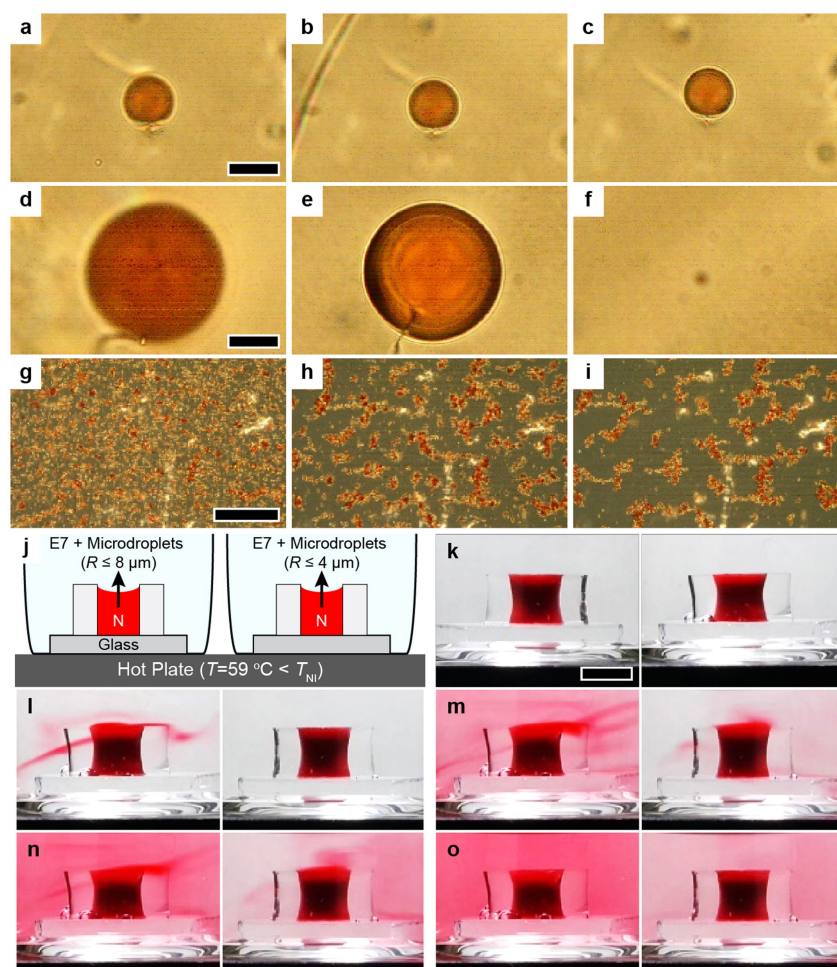
Extended Data Fig. 7 | Influence of the size and clustering of microdroplets on release from the LC. a–f, Optical micrographs of microdroplets ($C_{SDS} = 2$ mM and red tracer), with $R = 9.5$ μm (**a–c**) and 27 μm (**d–f**) in an LC (E7) at 25 °C (**a, d**), 50 °C (**b, e**) and 59 °C (**c, f**); $\rho_{E7} > \rho_{aq}$ and $C_{aq} = 1$ v%. Scale bars, 20 μm. The microdroplets were elastically trapped in the nematic LC bulk at 25 °C. As the temperature increased to 50 °C ($R > 34$ μm for release), the microdroplets moved upwards and into focus, but were not dispensed into the overlying water; the focal plane was near the interface between the LC and the overlying aqueous solution. At 59 °C ($R > 23$ μm for release), we observed the larger microdroplet ($R = 27$ μm) to escape into the overlying aqueous phase, whereas the smaller microdroplet ($R = 9.5$ μm) remained elastically trapped in the nematic bulk. This observation is in good agreement with

our theoretical prediction (Extended Data Fig. 5l, m). **g–i,** Micrographs of the clustering of microdroplets at 0 min (**g**), 30 min (**h**) and 180 min (**i**) after they were dispersed in the LC; $C_{aq} = 2$ v% ($C_{SDS} = 9$ mM). Scale bar, 200 μm. **j–o,** Illustration (**j**) and sequential micrographs (**k–o**) of thermally triggered, continuous release of microdroplets ($C_{SDS} = 9$ mM and red tracer) from mini-wells filled with E7 containing microdroplets of different sizes, at 0 min (**k**), 7 min (**l**), 10 min (**m**), 12 min (**n**) and 15 min (**o**) after the baths were heated to $T_h = 59$ °C($< T_{NI}$); $\rho_{E7} > \rho_{aq}$ ($F_b > 0$) and $C_{aq} = 20$ v%. Scale bar, 5 mm. The mini-well containing the larger microdroplets (left bath) exhibited a higher release rate due to the facile formation of microdroplet clusters with a radius higher than that for which $F_b^{net} > 0$, consistent with the theoretical model whose results are shown in Extended Data Fig. 5l, m.

Extended Data Fig. 8 | Role of electrical double-layer interactions in the release of microdroplets from an LC. a, Calculated repulsive elastic (F_{e1}, dashed line) and attractive electrical double-layer (F_{edl}, solid lines) forces acting on a microdroplet ($C_{SDS} = 9$ mM, $R = 1.5$ μm) as a function of h_1 following the addition of DTAB with $C_{DTAB} = 10$ mM (red), 5 mM (orange) and 2 mM (black) to the overlying aqueous phase. The inset shows the corresponding net forces ($F_i^{net} = F_{e1} + F_{edl}$). **b**, F_i^{net} near the interface between the LC and the overlying aqueous phase ($h_1 = \lambda$), and initial release rate of microdroplets (from 0 to 60 min in Fig. 2g) as a function of C_{DTAB} added into the overlying aqueous phase. **c**, Illustration of inverted mini-wells in baths with water (pH 7, left bath) and alkaline water (pH 13, right bath) at $T = 45$ °C ($> T_{NI}$). **d, e**, Sequential photographs of mini-wells filled with 5CB containing aqueous microdroplets (red tracer) at 0 min (**b**) and 60 min (**c**) after an N-to-I phase transition, with $C_{aq} = 10$ v% ($C_{SDS} = 9$ mM) and $T_h = 50$ °C. Scale bar, 5 mm. Because $\rho_{LC} < \rho_{aq}$ ($F_b < 0$), tracers are continuously released from an isotropic phase of 5CB ($F_{e1} = 0$) into the pure water (left bath). In the alkaline water (right bath), however, the release is suppressed because of the introduction of repulsive charge interactions between the LC interface in alkaline water (negatively charged) and SDS-containing aqueous microdroplets (negatively charged).
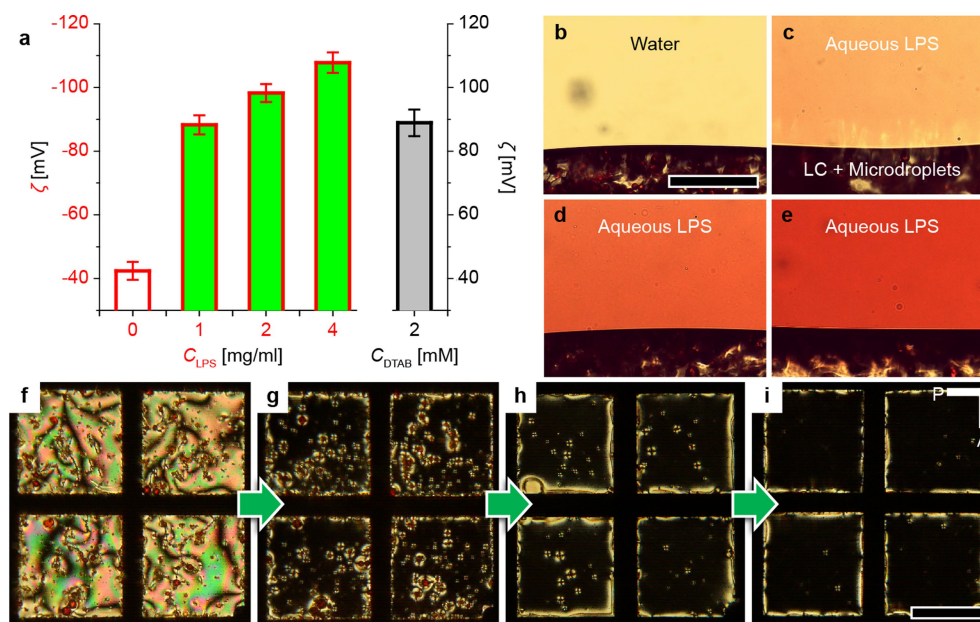
Extended Data Fig. 9 | Triggering of the release of dispersed microdroplets by interfacial charge interactions of biological molecules. a, Zeta potential ζ at LC–aqueous interface without (white bar) and with lipopolysaccharides (LPS; green bars) from *Escherichia coli*, or with DTAB (grey bar). The data are mean values and the error bars are 1 s.d. ($n > 3$). **b–e**, Micrographs (side view) showing the ejection of microdroplets ($C_{DTAB} = 2\,mM$ and red tracer) from LC (5CB) 30 min after addition of $C_{LPS} = 0\,mg\,ml^{-1}$ (**b**), 1 mg ml^{-1} (**c**), 2 mg ml^{-1} (**d**) and 4 mg ml^{-1} (**e**) to the overlying aqueous phase. **f–i**, Sequential micrographs

(top view) showing the ejection of microdroplets before (**f**) and at 0 min (**g**), 15 min (**h**) and 30 min (**i**) after the addition of $C_{LPS} = 4\,mg\,ml^{-1}$ into the overlying aqueous phase. Scale bars, 200 μm. P and A indicate the orientations of the polarizer and analyser, respectively. In the presence of LPS, microdroplets are ejected continuously from the LC, as evidenced by the release of red tracer (**b–e**) and the decrease in the population of aqueous microdroplets within the thin LC film (40 μm in thickness; **f–i**). The release rate is enhanced with an increase in C_{LPS} (**b–e**), consistent with release controlled by interfacial charge interactions.
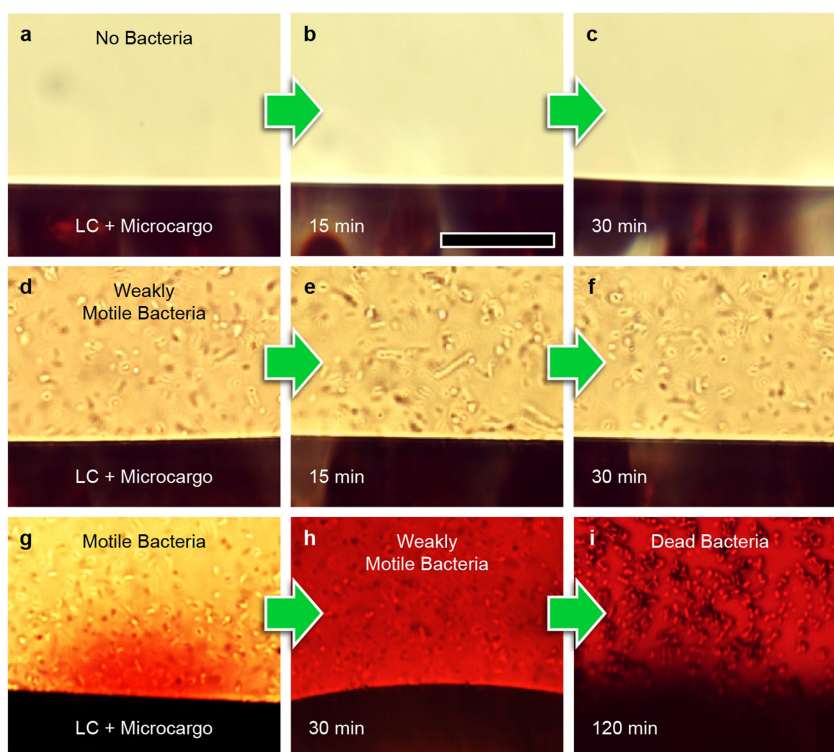
Extended Data Fig. 10 | Ejection of microdroplets from the LC by motile bacteria. a–f, Sequential micrographs showing that microdroplets containing anti-bacterial agent (2 mM DTAB and 1 wt% silver acetate) are not ejected from the LC (5CB) in the absence of bacteria (**a–c**) and at 0 min (**a, d**), 15 min (**b, e**) and 30 min (**c, f**) after the arrival of weakly motile bacteria (**d–f**); $C_{aq} = 10$ v%. **g–i,** Sequential micrographs showing ejection of microdroplets from the LC at 0 min (**g**), 30 min (**h**) and 120 min (**i**) after the arrival of motile bacteria and subsequent bacterial death and aggregation. Scale bar, 40 μm. **g,** Motile bacteria generate shear stresses at the LC interfaces, triggering the release of microdroplets containing anti-bacterial agent. **h,** As the anti-bacterial agents are released, the bacteria become less motile. At 30 min, we observe dead bacteria and cessation of the triggered release due to the decrease in the number of motile bacteria. The amount of silver acetate released is 1–2 μg μl^{-1}. **i,** Two hours after the arrival of motile bacteria, only dead (non-motile) bacteria are observed.
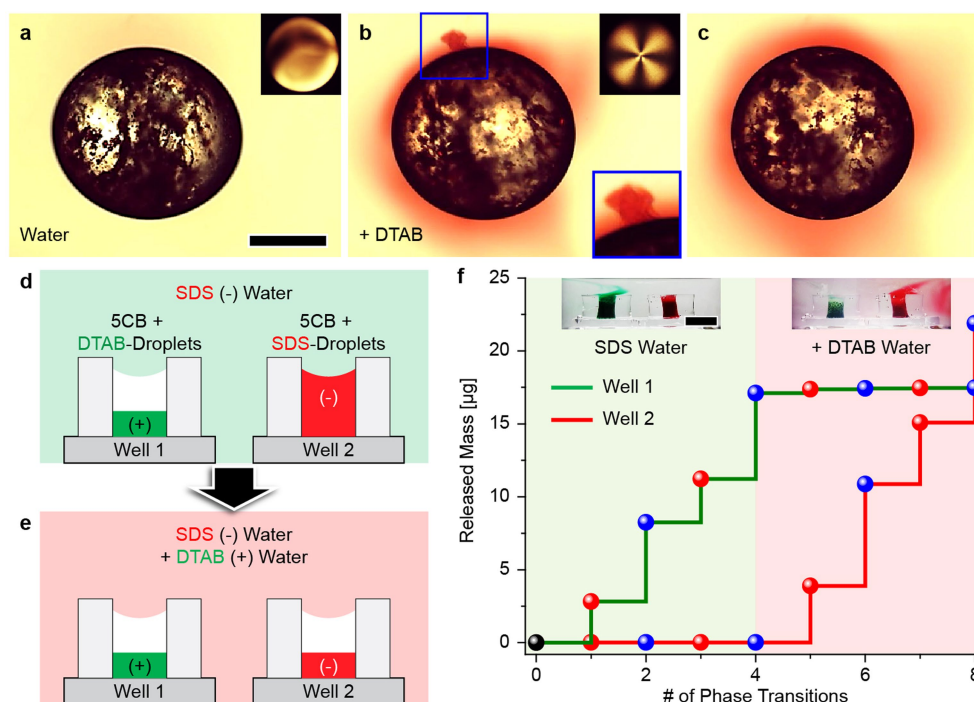
Extended Data Fig. 11 | LC systems with complex geometries and responsiveness to multiple stimuli. a–c, Isothermal release of aqueous microdroplets ($C_{SDS} = 9$ mM and red tracer) from a large LC emulsion droplet (5CB) before (**a**) and at 50 s (**b**) and 80 s (**c**) after the addition of DTAB (10 mM) into surrounding aqueous phase; $C_{aq} = 5$ v%. Scale bar, 200 μm. The insets in **a** and **b** are optical micrographs (crossed polars) of the LC droplet, showing the optical response. **d–f,** Selective release of two agents, triggered by a combination of chemical and thermal stimuli (see Methods for details). **d,** In an aqueous SDS bath, the thermal stimulus triggers release of DTAB-doped microdroplets (green tracer) from Well 1, but not of SDS-doped microdroplets (red tracer) from Well 2 (1st to 4th phase transition; left inset in **f**). **e,** Addition of DTAB into the bath reverses the charge at the interface between the LCs and the overlying aqueous phase, thus enabling the ejection of microdroplets from Well 2, but not from Well 1 (5th to 8th phase transition; right inset in **f**). Red and blue points in **f** correspond to the released mass of tracers after N-to-I and I-to-N phase transitions, respectively. Scale bar, 5 mm.
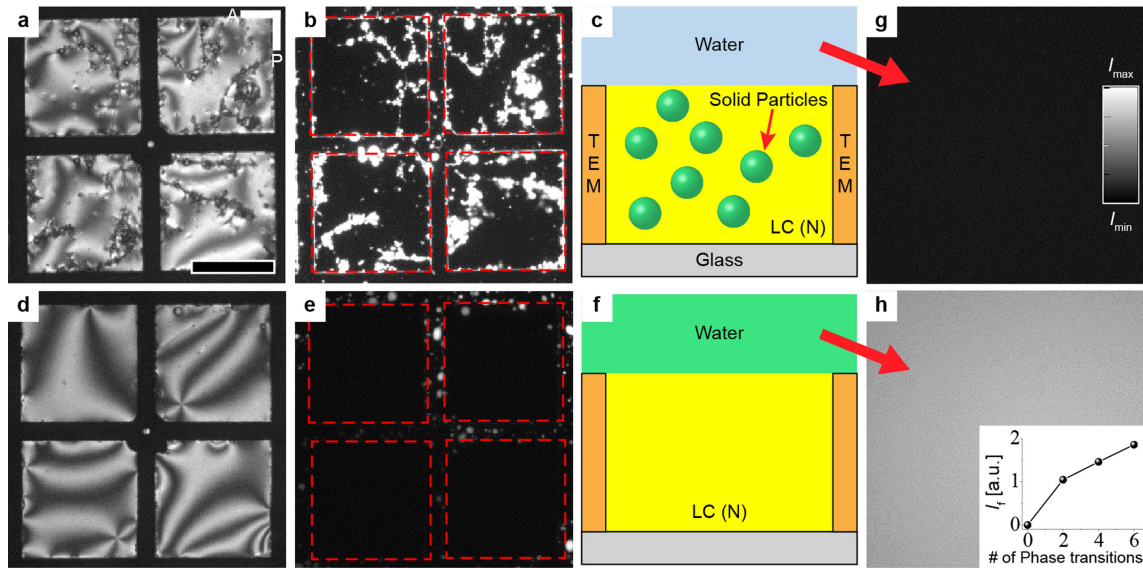
Extended Data Fig. 12 | Triggered release of water-soluble solid microparticles from an LC film. a–f, Polarizing (**a**, **d**; top view) and fluorescence (**b**, **e**; top view) micrographs and schematic illustrations (**c**, **f**; side view) of an LC film at 25 °C in the initial N phase (**a–c**) and after six phase transitions (**d–f**) with $T_h = 50$ °C and $T_c = 25$ °C. Scale bar, 200 μm. The LC film (5CB, 40 μm in thickness) contained solid microparticles of FITC-dextran (1–2 wt%). Before any phase transition, a strong fluorescence signal was detected from the FITC-dextran microparticles that were sequestered in the LC film (**b**), but not from the water bath (**g**), indicating that the solid microparticles were trapped in the LC. After six N–I phase transitions, however, no fluorescence signal was detected from the LC (**e**), whereas the water bath showed a strong fluorescence signal (**h**). The inset in **h** shows the fluorescence intensity I_f from the bath as a function of the number of phase transitions.